Monthly Notices
of the
ROYAL ASTRONOMICAL SOCIETY

MNRAS **478,** 4720–4737 (2018)
Advance Access publication 2018 May 7

doi:10.1088/mnras/sty1193

Unmasking the hidden NGTS-3Ab: a hot Jupiter in an unresolved binary system

Maximilian N. Günther,[1★] Didier Queloz,[1,2] Edward Gillen,[1] Laetitia Delrez,[1] François Bouchy,[2] James McCormac,[3,4] Barry Smalley,[5] Yaseen Almleaky,[6,7] David J. Armstrong,[3,4] Daniel Bayliss,[3] Artem Burdanov,[8] Matthew Burleigh,[9] Juan Cabrera,[10] Sarah L. Casewell,[9] Benjamin F. Cooke,[3,4] Szilárd Csizmadia,[10] Elsa Ducrot,[8] Philipp Eigmüller,[10,11] Anders Erikson,[10] Boris T. Gänsicke,[3,4] Neale P. Gibson,[12] Michaël Gillon,[8] Michael R. Goad,[9] Emmanuël Jehin,[8] James S. Jenkins,[13,14] Tom Louden,[3,4] Maximiliano Moyano,[15] Catriona Murray,[1] Don Pollacco,[3,4] Katja Poppenhaeger,[12] Heike Rauer,[10,11,16] Liam Raynard,[9] Alexis M. S. Smith,[10] Sandrine Sohy,[8] Samantha J. Thompson,[1] Stéphane Udry,[2] Christopher A. Watson,[12] Richard G. West[3] and Peter J. Wheatley[3,4]

Affiliations are listed at the end of the paper

Accepted 2018 May 2. Received 2018 May 2; in original form 2018 March 13

ABSTRACT

We present the discovery of NGTS-3Ab, a hot Jupiter found transiting the primary star of an unresolved binary system. We develop a joint analysis of multicolour photometry, centroids, radial velocity (RV) cross-correlation function (CCF) profiles, and their bisector inverse slopes (BIS) to disentangle this three-body system. Data from the Next Generation Transit Survey (NGTS), SPECULOOS and HARPS are analysed and modelled with our new BLENDFITTER software. We find that the binary consists of NGTS-3A (G6V-dwarf) and NGTS-3B (K1V-dwarf) at <1 arcsec separation. NGTS-3Ab orbits every 1.675 d. The planet radius and mass are $R_{\rm planet} = 1.48 \pm 0.37$ R$_{\rm J}$ and $M_{\rm planet} = 2.38 \pm 0.26$ M$_{\rm J}$, suggesting it is potentially inflated. We emphasize that only combining all the information from multicolour photometry, centroids and RV CCF profiles can resolve systems like NGTS-3. Such systems cannot be disentangled from single-colour photometry and RV measurements alone. Importantly, the presence of a BIS correlation indicates a blend scenario, but is not sufficient to determine which star is orbited by the third body. Moreover, even if no BIS correlation is detected, a blend scenario cannot be ruled out without further information. The choice of methodology for calculating the BIS can influence the measured significance of its correlation. The presented findings are crucial to consider for wide-field transit surveys, which require wide CCD pixels (>5 arcsec) and are prone to contamination by blended objects. With TESS on the horizon, it is pivotal for the candidate vetting to incorporate all available follow-up information from multicolour photometry and RV CCF profiles.

Key words: surveys – eclipses – occultations – planets and satellites: detection – binaries: eclipsing.

★ E-mail: mg719@cam.ac.uk

1 INTRODUCTION

To date, more than 3700 exoplanets have been found, 2800 of which with the transit technique.[1] Out of these, we currently know 88 (24) extra-solar binary systems (multiple systems), which contain a total of 125 (34) exoplanets[2] (Schwarz et al. 2016). The Next Generation Transit Survey (NGTS; Wheatley et al. 2018) and the upcoming Transiting Exoplanet Survey Satellite (TESS; Ricker et al. 2014) will soon further increase the sample of small planets orbiting bright stars, delivering prime targets for follow-up studies. Naturally, such wide-field exoplanet surveys require wide CCD pixels (>5 arcsec). This can influence the observation in two ways: (1) circa 44 per cent of main-sequence F6–K3 systems (Raghavan et al. 2010) and 20 per cent–50 per cent of late K and M dwarfs (Ward-Duong et al. 2015; Fischer & Marcy 1992) are actually binary and triple systems. A given target might hence be a multistar system, whose companions remain unresolved. (2) A single CCD pixel often contains multiple background objects, whose light (and signals) influence the observations. Both scenarios can lead to the underestimation of planet radii or to false positives (see e.g. Cameron 2012). The most common false positives are unresolved eclipsing binaries (EBs) with grazing eclipses or low-mass companions, which both can cause a shallow, planet-like transit signal. Another class is background eclipsing binaries (BEBs). These are faint and distant EBs aligned along the line of sight of a bright target star. This dilutes their signal on to a planetary scale.

False positives typically outnumber the planet yield by a factor of 100 (see e.g. Almenara et al. 2009; Latham et al. 2009; Hartman, Bakos & Torres 2011). We previously predicted for NGTS that initially ∼5600 such false positives will outnumber the yield of ∼300 new exoplanets (Günther et al. 2017a). A series of sophisticated vetting tools have recently been developed for identifying blend scenarios and disentangling planets from false positives (see e.g. Torres et al. 2010b; Morton 2012; Díaz et al. 2014; McCauliff et al. 2015; Santerne et al. 2015; Torres et al. 2015; Coughlin et al. 2016; Günther et al. 2017b; Armstrong et al. 2018).

In this paper, we evaluate an interesting signal observed with NGTS, that initially seemed to originate from the transit of a hot Jupiter around a Sun-like star. After gathering follow-up spectroscopy with the High Accuracy Radial velocity Planet Searcher (HARPS), a planet-like radial velocity (RV) signal was confirmed, but a bisector correlation was detected. Usually, bisector correlations were seen as indicators of BEBs, and as such the system was nearly disregarded as a false positive. Through careful analysis of all data and false positive scenarios and development of a new routine, our BLENDFITTER modelling toolbox, we are able to disentangle this system.

We here present the discovery of NGTS-3Ab, a hot Jupiter found orbiting a star in a still visually unresolved binary system. This paper attempts to provide a comprehensive case study to unmask an unresolved three-body system by combining all information from multicolour photometry, centroids, RV measurements, and their bisectors. This study is based on data gathered with the NGTS, SPECULOOS (Search for habitable Planets EClipsing ULtra-cOOl Stars, in commissioning; Burdanov et al. 2017 and Gillon et al. in preparation) and HARPS (Mayor et al. 2003), and enhanced by our recent advances with the centroiding technique for NGTS (Günther et al. 2017b). We here develop a new routine, BLENDFITTER to conjointly model multicolour photometry, centroids and the RV extraction process. For this, we simulate the RV cross-correlation functions (CCFs) and study correlations of the bisector inverse span (BIS). Our study highlights the value of a thorough inspection and modelling of multicolour photometry, centroids, RV CCFs, and BISs for exoplanet surveys.

[1] http://exoplanetarchive.ipac.caltech.edu/, online 2018 March 09.
[2] http://www.univie.ac.at/adg/schwarz/multiple.html, online 2018 March 09.

Table 1. Summary of all observations of NGTS-3 used in this work, including the discovery photometry, the follow-up photometry and the spectroscopic observations.

Facility	Date	Notes
NGTS	2016 Aug 18–2017 Dec 6	78572 points 10 s exp.
SPECULOOS-Callisto	2018 Jan 26	301 points *r*' - 30 s exp.
SPECULOOS-Io	2018 Feb 9	471 points *i*'+*z*' - 30 s exp.
SPECULOOS-Europa	2018 Feb 9	457 points *i*'+*z*' - 30 s exp.
SPECULOOS-Callisto	2018 Feb 15	445 points *g*' - 35 s exp.
SPECULOOS-Europa	2018 Feb 15	469 points *r*' - 30 s exp.
HARPS	2017 Feb 1–2017 Mar 5	7 spectra

Table 2. NGTS photometry and centroid data for NGTS-3. The full table is available in a machine-readable format from the online journal. For guidance, 10 observations are shown here.

Time (d) (HJD–2450000)	Flux (normalized)	Centroid *x* (pixel)	Centroid *y* (pixel)
...	...	...	...
7619.901516	1.021527545	−0.11709990	0.06187227
7619.901667	1.000179888	−0.04072431	0.04446441
7619.901806	0.957097368	−0.02046733	0.04210692
7619.901956	1.076526278	0.07883140	0.03817588
7619.902106	0.996836033	−0.03235835	0.03558102
7619.902257	1.123472365	0.10736324	0.00703842
7619.902419	1.010499832	0.09472378	−0.01132131
7619.902569	0.943342956	−0.06200864	0.05012148
7619.90272	1.019069713	−0.00554865	−0.03038287
7619.90287	0.961933312	0.03336356	−0.09503899
...	...	...	...

2 OBSERVATIONS

NGTS-3 (NGTS J061746.7-354222.9; see Table 5) was photometrically discovered by NGTS, and followed up using high precision photometry from SPECULOOS during its commissioning period, and spectroscopy from HARPS. We detail all of these observations in this section and provide a summary in Table 1.

2.1 NGTS photometry

NGTS is a fully robotized array of twelve 20 cm Newtonian telescopes based at European Southern Observatory (ESO)'s Paranal Observatory in Chile. The telescopes are equipped with 2K×2K e2V deep-depleted Andor IKon-L CCD cameras with 13.5 μm pixels, corresponding to an on-sky size of 4.97 arcmin.

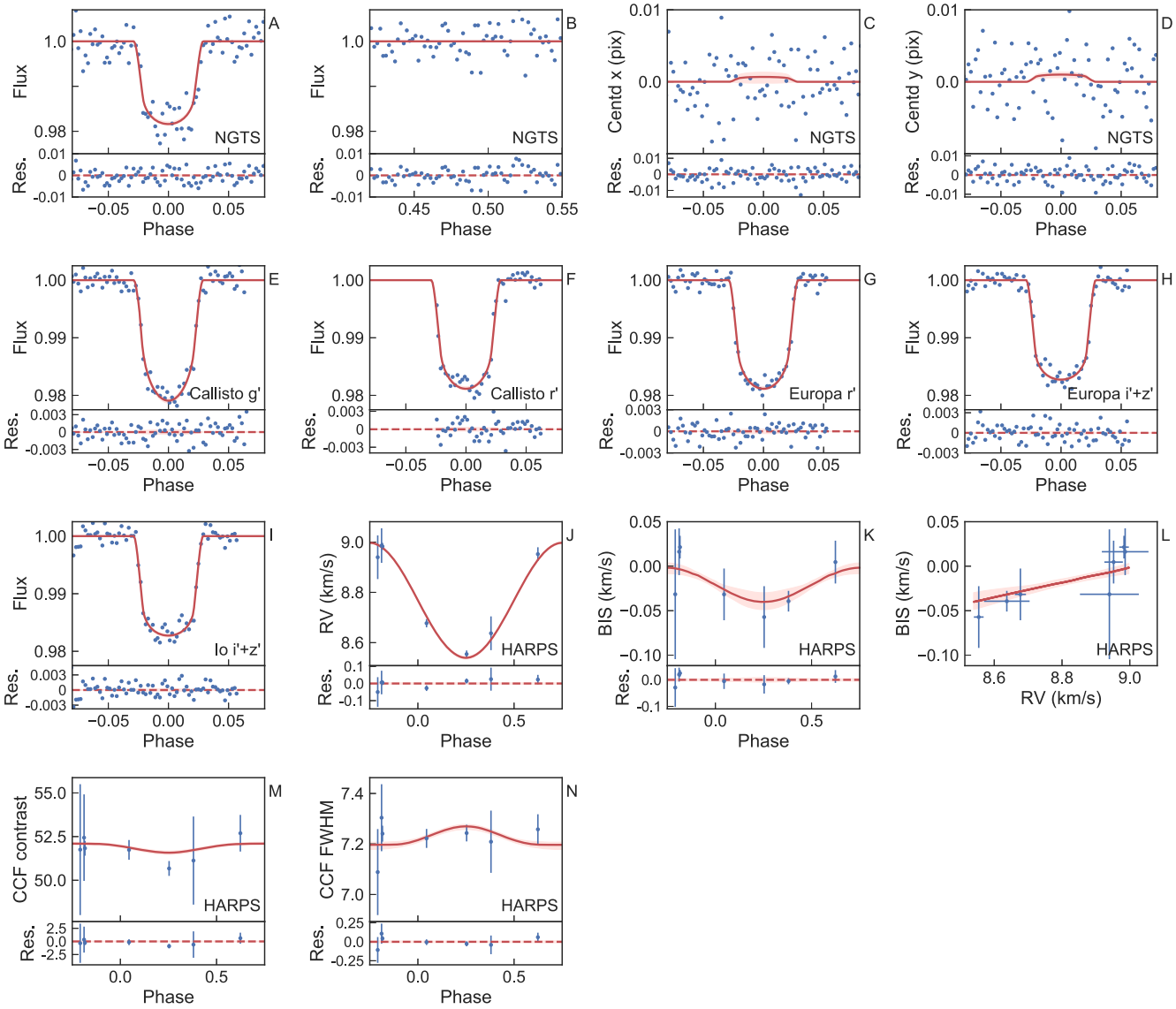

Figure 1. Data for NGTS-3, phase-folded at the best-fitting period of 1.675 d. (a) NGTS light curve, (b) NGTS light curve around phase 0.5, (c) NGTS centroid in *x*, (d) NGTS centroid in *y*, (e) SPECULOOS Callisto *g*' band, (f) SPECULOOS Callisto *r*' band, (g) SPECULOOS Europa *r*' band, (h) SPECULOOS Europa *i*'+*z*' band, (i) SPECULOOS Io *i*'+*z*' band, (j) HARPS RV (RV) measurements, (k) HARPS BIS, (l) HARPS BIS versus RV, (m) HARPS contrast measurements, and (n) HARPS FWHM measurements. Photometric measurements are binned equally in phase with a spacing of 0.002 (total of 500 phase-folded points). We randomly draw 100 samples from the MCMC chain and calculate the models. Red curves in (a)–(n) display the median and 16th/84th percentile of all drawn models. The global, joint modelling is described in Section 3.8.

The presented data on NGTS-3 were observed on a single NGTS telescope over a photometric campaign conducted between 2016 August 18 and December 06, and detrended with the 'TEST18' pipeline version. This contains 78 572 exposures of 10 s in the NGTS bandpass (550–927 nm) over a total of 89 observation nights. The telescope was autoguided using an improved version of the DONUTS autoguiding algorithm (McCormac et al. 2013). The rms of the field tracking errors was 0.136 pixels over the 89 nights. This slightly elevated rms (compared to the typical value of ∼0.05 pixels) was due to a mechanical issue with the right ascension bearing in the mount, whereby the telescope occasionally jumped by ∼1 pixel. The autoguiding then recentred the field after few exposures.

Image reduction, aperture photometry, and reduction of systematic effects were performed with the NGTS data pipelines described in Wheatley et al. (2018). These are based on implementations of the CASUTOOLS[3] and SYSREM packages (Tamuz, Mazeh & Zucker 2005). Light curves were screened for transit-like signals using ORION, an implementation of the box-fitting least-squares method (Kovács, Zucker & Mazeh 2002). We further extracted and reduced the flux centroids of NGTS-3 as described in Günther et al. (2017b). A centroid shift correlated to a transit-like signal is an indicator for contamination by a fainter background source.

NGTS-3's transit-like signal of 2 per cent was detected with a period of 1.675 d and width of 2 h. No centroid shift was detected. Initially, these photometric observations alone made NGTS-3 a strong hot Jupiter candidate.

[3]http://casu.ast.cam.ac.uk/surveys-projects/software-release, online 2018 March 09.

Table 3. SPECULOOS Callisto *r*'-band photometry for NGTS-3. The full table, and tables for the remaining SPECULOOS observations with Europa, Io, and Callisto, are available in a machine-readable format from the online journal. For guidance, 10 observations are shown here.

Time (d) (HJD–2450000)	Flux (normalized)	Flux error (normalized)
8144.51886	0.99634245	0.00306679
8144.51931	0.99873645	0.00303029
8144.51976	0.9895214	0.00292396
8144.52021	0.99279671	0.0029041
8144.52067	0.99233135	0.00286985
8144.52112	0.99131786	0.00286618
8144.52157	0.98893842	0.00277872
8144.52202	0.99065349	0.00284851
8144.52247	0.98691918	0.00285377
8144.52292	0.98281773	0.00297856
...	...	...

Table 2 provides the full photometry and centroid time series after detrending. Fig. 1 shows these data phase-folded at the best-fitting transit period as determined via our global modelling (outlined in Section 3.8).

2.2 SPECULOOS photometry

SPECULOOS (Burdanov et al. 2017; Gillon et al. in preparation) is located at ESO's Paranal Observatory in Chile and currently undergoing commissioning. The facility consists of four robotic 1-m Ritchey–Chretien telescopes. Each telescope is equipped with an Andor Peltier-cooled deeply depleted 2K×2K CCD camera with a 13.5 μm pixel size. The field of view of each telescope is 12 arcmin × 12 arcmin (0.35 arcsec pixel^{-1}), with optimal sensitivity in the near-infrared (700–1000nm).

We observed NGTS-3 in the *g*', *r*', and *i*'+*z*' bands during the commissioning of the first three SPECULOOS telescopes, Europa, Io, and Callisto. A summary of these observations is provided in Table 1. The images were calibrated using standard procedures (bias, dark, and flat-field correction) and photometry was extracted using the IRAF/DAOPHOT aperture photometry software (Stetson 1987), as described by Gillon et al. (2013). For each observation, a careful selection of both the photometric aperture size and stable comparison stars was performed manually to obtain the most accurate differential light curve of NGTS-3. Table 3 provides the full photometry of one of the observations as an example. Figs 1e-i show the data with the best fit determined via our global modelling (see Section 3.8).

2.3 HARPS spectroscopy

We obtained RV follow-up for NGTS-3 with HARPS (Mayor et al. 2003) on the ESO 3.6 m telescope at La Silla Observatory in Chile between 2017 February 01 and March 05. Data were reduced using the standard HARPS reduction pipeline. RVs were calculated for each epoch via cross-correlation of the HARPS data reduction pipeline with a G2 mask. Results along with their associated error, full width at half-maximum (FWHM), contrast, and bisector slope are listed in Table 4 . Early RV results were encouraging, with an in-phase variation of $K \approx 230$ m s^{-1} at a very high significance (see Fig. 1j). However, the bisector span of the RV CCF showed a strong correlation with the measured RV (see Figs 1k and l). This

Table 4. HARPS RVs for NGTS-3 as retrieved by the standard data reduction software (HARPS DRS 3.5). The full table is available in a machine-readable format from the online journal.

Time (d) HJD–2450000	RV (km s^{-1})	RV error (km s^{-1})	FWHM (km s^{-1})	Contrast (per cent)	BIS (km s^{-1})
7785.721175	8.98228	0.01635	7.23903	52.138	0.02101
7790.705903	8.93196	0.02892	7.00693	51.672	−0.00334
7791.692363	8.62082	0.01606	7.08774	50.959	−0.04371
7811.584627	8.55463	0.01448	7.2421	51.021	−0.05955
7814.586319	8.67687	0.01237	7.22015	52.134	−0.01864
7815.555984	8.94451	0.01069	7.22257	52.785	0.01179
7817.545532	8.98783	0.01712	7.24024	52.212	0.01667

Table 5. Stellar properties for the NGTS-3 system.

Property	Value	Source
Astrometric properties of the system		
RA	94.444801	2MASS
Dec.	−35.706394	2MASS
NGTS ID	J061746.7–354222.9	NGTS
2MASS ID	J06174675–3542230	2MASS
Gaia DR2 ID	2885350546895266432	Gaia DR2
μ_{RA} (mas yr^{-1})	-7.4 ± 1.2	UCAC5
$\mu_{Dec.}$ (mas yr^{-1})	8.6 ± 1.3	UCAC5
Photometric properties of the system		
V (mag)	14.642 ± 0.047	APASS
B (mag)	15.451 ± 0.049	APASS
g (mag)	15.002 ± 0.028	APASS
r (mag)	14.423 ± 0.043	APASS
i (mag)	14.252 ± 0.01	APASS
G_{GAIA} (mag)	14.488	Gaia DR2
NGTS (mag)	14.109	This work
J (mag)	13.281 ± 0.029	2MASS
H (mag)	12.965 ± 0.029	2MASS
K (mag)	12.814 ± 0.03	2MASS
*W*1 (mag)	12.798 ± 0.023	WISE
*W*2 (mag)	12.820 ± 0.023	WISE
B−*V* colour	0.809 ± 0.068	APASS
J−*H* colour	0.316 ± 0.042	2MASS
H−*K* colour	0.151 ± 0.042	2MASS
Derived properties for NGTS-3A		
$T_{eff,\,A}$ (K)	5600 ± 150	HARPS spectra
$T_{eff,\,A}$ (K)	5570 ± 140	IRFM fitting
$[Fe/H]_A$	$+0.12 \pm 0.15$	HARPS spectra
$(v \sin i)_A$ (km s^{-1})	1.0 ± 0.7	HARPS spectra
$\log g_A$	4.5 ± 0.2	HARPS spectra
$\log A(\mathrm{Li})_A$	<1.1	HARPS spectra
M_A ($M_\odot$)	1.017 ± 0.093	ER
R_A ($R_\odot$)	0.93 ± 0.23	ER
ρ_A (g cm^{-3})	1.09 ± 0.29	ER
Spectral type, A	G6V (G2V-G8V)	ER2

Notes: Two Micron All Sky Survey (2MASS; Skrutskie et al. 2006); United States Naval Observatory CCD Astrograph Catalog 5 (UCAC5; Zacharias, Finch & Frouard 2017); American Association of Variable Star Observers Photometric All-Sky Survey (APASS; Henden & Munari 2014); Wide-field Infrared Survey Explorer (WISE; Wright et al. 2010); *Gaia* (Gaia Collaboration et al. 2016, 2018); ER: empirical relations using Torres et al. (2010a); and ER2: empirical relations using Pecaut & Mamajek (2013).

can often be a sign of a contaminating spectrum with large RV shifts (e.g. due to a blended binary), which is responsible for the apparent RV variation of the target (Santos et al. 2002, see section 3.3).

3 ANALYSIS

3.1 Stellar properties

The NGTS-3 system is located at RA = 06h 17m 46.8s, Dec. = −35d 42m 22.3s, and is identified as NGTS J061746.7–354222.9, 2MASS J06174675–3542230, and Gaia 2885350546895266432 (DR2), with magnitudes $G = 14.4$, $J = 13.3$, and $K = 12.8$ (Table 5).

When analysing the HARPS data, we find a clear bisector correlation (Figs 1k and l). A positive correlation is a direct indicator for contamination of the spectrum of NGTS-3A by at least one other stellar object in the system (see Section 3.3). We perform a spectral fit of the seven obtained HARPS spectra to determine the parameters of the brightest object in the aperture, which we denote as NGTS-3A (Table 5). The overall signal-to-noise ratio (S/N) is relatively low (23:1), leading to large uncertainties on the derived parameters. The co-added spectrum shows no sign of contamination due to the other star in the aperture. Using methods similar to those described by Doyle et al. (2013), we determined values for the stellar effective temperature $T_{\rm eff,\,A}$, surface gravity $\log g_{\rm A}$, the stellar metallicity $[{\rm Fe/H}]_{\rm A}$, and the projected stellar rotational velocity $(v \sin i)_{\rm A}$. To constrain the latter, we obtained a macroturbulence value of $2.7\,{\rm km\,s^{-1}}$ using the Doyle et al. (2014) astereoseimic calibration. We find that the effective temperature of $T_{\rm eff,\,A} = 5600 \pm 150$ K from the spectra analysis, is consistent with our results using the infrared flux method (IRFM). Lithium is not seen in the spectra, giving an upper limit of $\log A({\rm Li})_{\rm A} < 1.1$. We conclude from the measured $T_{\rm eff,\,A}$ that NGTS-3A is most likely a G6V dwarf, but consistent with a G2V–G8V dwarf (see e.g. Pecaut & Mamajek 2013).

3.2 Centroiding

NGTS-3 is registered as a single source in all existing archival data. As part of the NGTS candidate vetting pipeline, we employ our centroiding technique (Günther et al. 2017b) to all targets. This test is able to detect shifts in the photometric centre of flux during transit events at the sub-milli-pixel level. It can identify blended EBs at separations below 1 arcsec, well below the size of individual NGTS pixels (4.97 arcsec). We previously estimated that this enables the identification of ∼80 per cent of BEBs before follow-up.

We do not observe any centroid shift for NGTS-3 (Fig. 2, Table 6). Concurring with the NGTS photometry, this initially made a planet scenario very likely. We emphasize that the non-detection of a centroid shift minimizes the risk of blends, but only completely rules out blends at more than ∼1 arcsec separation (dependent on the magnitude difference and signal depth). In any case, the non-detection of a centroid shift allows us to place upper limits on the possible location of this blend and the dilution it causes.

3.3 HARPS CCF, RV, and bisector model

The RV of a star is measured as the Doppler shift of spectral lines. For this, the stellar spectrum is obtained and then cross-correlated with a reference spectrum. The peak of the CCF gives the RV. In practice, it is fitted with a Gaussian function, whose mean value is the reported RV value. Likewise, the FWHM and amplitude of the Gaussian (contrast) can be extracted. The left-hand column in

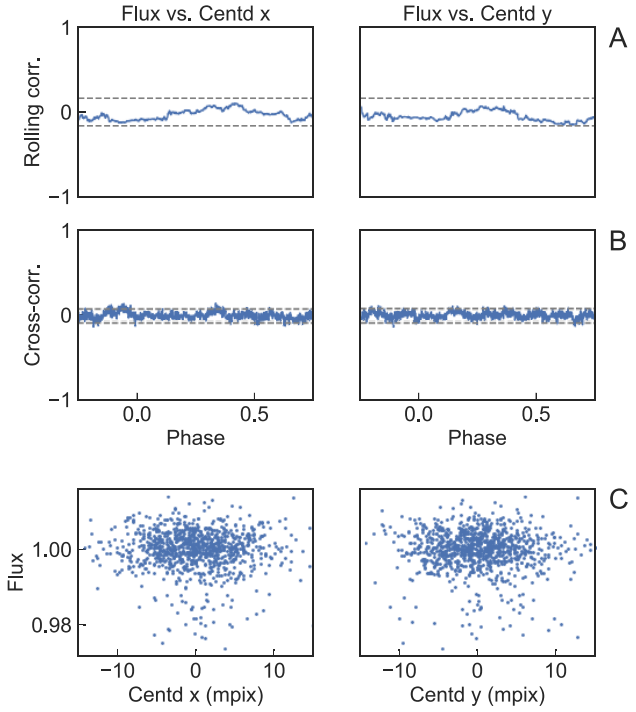

Figure 2. No identification of a centroid shift correlated to the transit signal for NGTS-3Ab. The upper panels show the (a) rolling (window) correlation and (b) cross-correlation between flux and centroid, phase-folded on the best-fitting transit period. Neither shows signs of a correlation. Dashed lines indicate the 99 per cent confidence intervals in each case. Panel (c) shows the 'rain plots', a graphical illustration of the relation between flux and centroids (see e.g. Batalha et al. 2010; Günther et al. 2017b). Here, the 'rain' falls straight down, meaning there is no sign of a correlation.

Table 6. No statistical identification of a centroid shift in NGTS-3. The table displays the S/N of the rolling correlation and cross-correlation analyses, which are well below our threshold S/N = 5 in all cases. Further the table lists the resulting p-values from a T-test and binomial test of the in-transit centroid data, testing the null hypothesis that the centroid is distributed around the mean of the out-of-transit data, i.e. around 0. All p-values are well above our threshold $p = 0.01$ for rejecting the null hypothesis.

	x	y
S/N rolling correlation	1.88	1.35
S/N cross-correlation	2.23	221
p-value T-test	0.0692	0.1672
p-value binomial test	0.0649	0.1189

Fig. 3 shows the seven CCFs obtained from cross-correlating our HARPS measurements with a reference spectrum of a G2-type star (HARPS DRS has the option of a K5 and G2 mask for cross-correlations).

The CCF bisector, in particular the BIS, has been proven to be a powerful tool to detect star spots (Queloz et al. 2001) and background binaries (Santos et al. 2002) that can mimic planet-like signals in RV data. The bisector is defined as the mean points half-way between equal intensities on both sides of the CCF peak. The BIS is defined as $v_{\rm t} - v_{\rm b}$, with $v_{\rm t}$ ($v_{\rm b}$) being the mean bisector velocity of all points between the top 10 per cent–40 per cent (the bottom 60 per cent–90 per cent) of the CCF peak depth (Queloz et al. 2001).

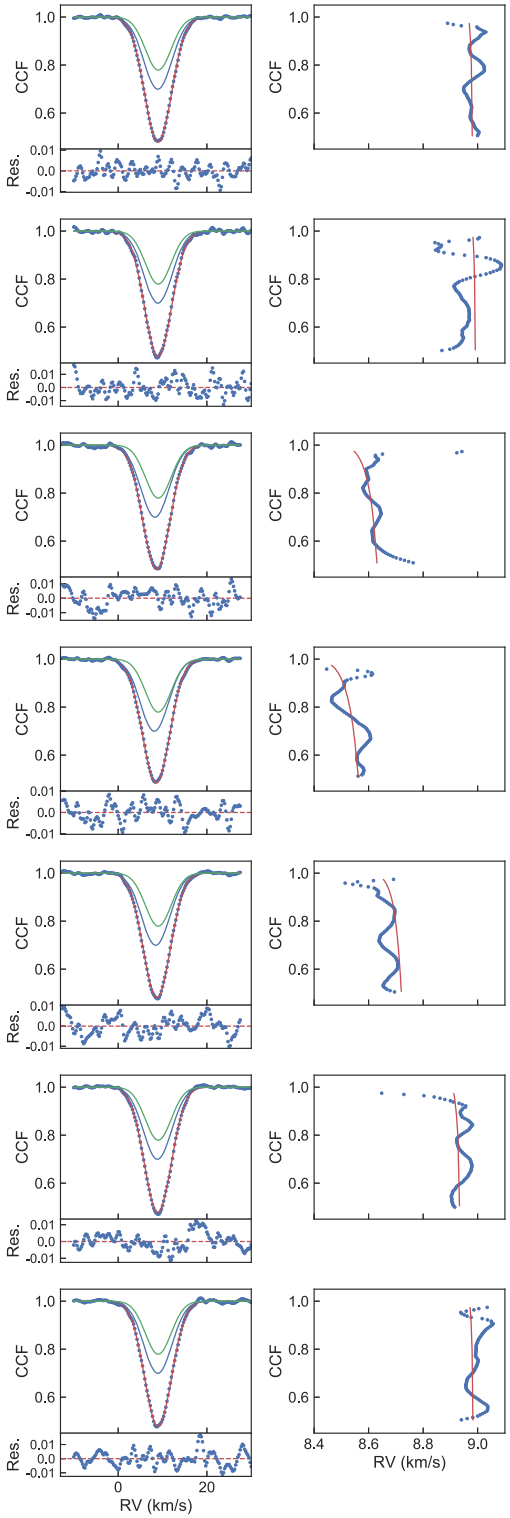

Figure 3. The seven HARPS CCF profiles (left-hand column), and zoom-on to their extracted bisectors (right-hand column). Left-hand column: the shown CCF profiles are corrected for the best-fitting baseline from the global BLENDFITTER MCMC model. Red lines show the MCMC results for the best fit of the movement of two stars, modelled as two Gaussian profiles. The model for star A is shown in green, star B in blue, and their sum in red. Sub-panels show the residuals of the fit. Right-hand column: bisectors were extracted by BLENDFITTER using the second derivatives of the Gaussian fit.

3.3.1 Comparison of approaches to extract the RV, FWHM, and contrast

The most recent HARPS data reduction software (HARPS DRS 3.5) fits an inverse Gaussian function with a constant baseline to the CCF profile. The RV, FWHM, and contrast measurements are then extracted as the mean, FWHM, and amplitude of the Gaussian. We implement two approaches in our BLENDFITTER code. The first choice follows the exact HARPS DRS procedure. As expected, our results match the HARPS results exactly, with a deviation of $<10^{-4}$. In all cases, this precision is by a factor of 100 within the parameters' error bars.

We find that the constant baseline approach of the HARPS DRS fit leaves strong systematic trends in the residuals of the CCF profiles. We hence implement a second method in our BLENDFITTER code. Instead of using a constant baseline, we employ a Gaussian process (GP) model jointly with our Gaussian fit and perform a Markov Chain Monte Carlo (MCMC) fit. The MCMC and GP are implemented using EMCEE (Foreman-Mackey et al. 2013) and GEORGE (Ambikasaran et al. 2016). A GP uses different kernels and metrics to evaluate the correlation between data points. The squared distance r^2 between data points x_i and x_j is evaluated for any metric M as

$$r^2 = (x_i - x_j)^T M^{-1} (x_i - x_j). \quad (1)$$

In our one-dimensional case, M is simplified to a scalar. We choose our GP kernel to be

$$k(r^2) = c(1 + 3\sqrt{r^2})e^{-3\sqrt{r^2}}, \quad (2)$$

which represents the product of a constant kernel c and a 'Matern 3/2 kernel'. This kernel can describe variations which display a rougher (i.e. more stochastic) behaviour in addition to a characteristic length scale, such as it is the case in the CCF profiles. We also fit for white noise.

We perform an MCMC fit for each CCF profile, using 50 walkers to explore the six dimensions (amplitude, mean, standard deviation, c, M, and a white noise scale factor). We run two separate burn-in phases of 2000 steps each, a third burn-in of 5000 steps, and an evaluation of 5000 steps. The maximum autocorrelation length for all data sets is <100 steps, and we hence consider all chains to be converged. We thin the chains by a factor of 10, which leads to a total of $50 \times 5000/10 = 25\,000$ samples.

Fig. 4 compares the resulting parameters from BLENDFITTER and HARPS DRS. Reported values and error bars are the median and 16th/84th percentile of the resulting posterior likelihood distributions. The GP approach improves the fit and reduces the systematic baseline trend visible in the residuals of the HARPS DRS approach. This shows that at the presence of strong systematics to the CCF profile, especially in the wings of the CCF profile, a constant baseline fit can be too restricting. This can lead to a high bias with low variance. The GP model allows an evaluation with lower bias and higher ('fairer') variance. We consequently use the parameters extracted with our GP model for the global modelling in Section 3.8. The full table of these values is available in a machine-readable format from the online journal.

We here purposely use a single Gaussian model to fit the measured HARPS CCF profiles. This is to match the standard way that HARPS data are analysed (assuming a single planet model). In contrast, in our global MCMC model (see Section 3.8), we outline the detailed analysis of the HARPS CCFs with a bimodal Gaussian model (for an unresolved blended system).

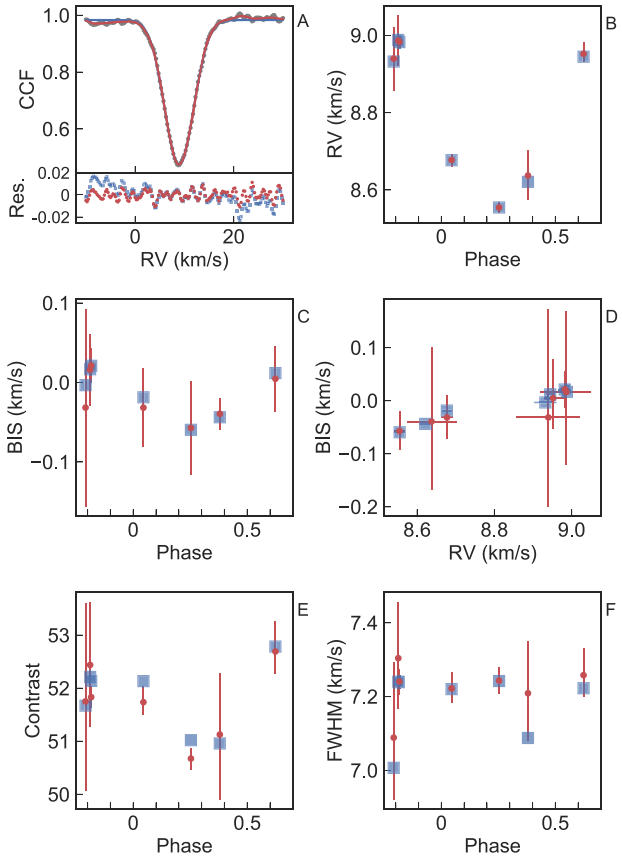

Figure 4. Comparison of the (a) fit and residuals and (b)–(f) the extracted parameters between the standard HARPS DRS pipeline with a constant baseline (DRS 3.5; blue squares), and our BLENDFITTER code using a GP model for the baseline (red circles). The latter allows an evaluation of the parameters and error bars which is less biased due to systematic noise in the wings of the CCF profile. Values and error bars are thereby estimated with an MCMC fit and represented as the median and 16th/84th percentile of the resulting posterior likelihood distributions.

3.3.2 *Comparison of approaches to extract the bisector and BIS*

Throughout the literature, the CCF bisectors have been calculated in slightly different ways, three of which we outline here. First, the original implementation for exoplanets by Queloz et al. (2001) builds on the approach used in studies of binary stars (e.g. Toner & Gray 1988; Gray 1989) for individual spectral lines. It uses the sampling on the left wing of the CCF peak. At each measured point a horizontal line is drawn to intersect with the right wing. The intersection value on the right wing is calculated from a linear interpolation between the two nearest points. The bisector at this level is then calculated as the mean between the left- and right-hand values. Second, a cubic spline interpolation can be used to interpolate both sides of the CCF, and calculate the bisector at any chosen value. Last, the most recent HARPS data reduction pipeline (HARPS DRS 3.5) further minimizes the impact of outlying points. The routine fits a Gaussian function to the CCF, and calculates the line bisectors from the second derivatives of this fit.

In our BLENDFITTER code, we implement these three methods of calculating the bisector: linear interpolation, cubic spline interpolation, and second derivatives of a Gaussian fit. We re-analyse the HARPS CCFs to verify our implementation reproduces the reported HARPS results, and to compare the three methods with each other. The right-hand column in Fig. 3 shows the extracted bisectors using the same approach as HARPS DRS. We note that all analysed HARPS spectra show a 'serpentine shape' in their bisectors, which can introduce systematic errors into the BIS calculation.

All three methods result in almost identical shapes of the bisectors. However, the linear interpolation approach leads to systematic deviations of the bisector near the top and bottom of the CCF profile. When extracting the BIS from the bisectors, we find that for low-noise CCF profiles all three methods agreed in their BIS measurements to a few metres per second, well within their error bars. However, for high-noise CCF profiles the cubic spline solution differed from the DRS approach by up to $\sim$10 m s^{-1}, and the linear interpolation approach by up to $\sim$100 m s^{-1}. This was mainly driven by the discrepancy in extracted bisectors towards the top and bottom of the CCF profile.

We detect a BIS correlation with all three methods. The DRS approach proves to be the most robust way to extract the BIS, while the linear interpolation is strongly affected by noise in the CCF profile. Our BLENDFITTER software includes the choice between all three methods, but as the DRS approach proved to be the most robust, we use this setting for all following analyses. We strongly caution that the choice of methodology for calculating the bisectors can influence the measured significance of a BIS correlation.

3.3.3 *BIS correlations: distinguishing atmospheric phenomena and blends*

If the target was a single star with no atmospheric phenomena, such as star spots, the entire CCF profile would oscillate around its mean value. Accordingly, the bisector would oscillate around its mean value, while maintaining its shape and orientation. Two events can cause a phase-dependent trend in the BIS: changes in the stellar atmosphere (Queloz et al. 2001) and blended objects (Santos et al. 2002).

Atmospheric phenomena: if a star shows strong atmospheric activity, such as star spots, the top of the RV CCF profile will remain mostly unaffected, while the bottom will show strong oscillations around the mean value. This leads to an anticorrelation between the BIS and RV measurements (see e.g. Queloz et al. 2001; Boisse et al. 2011).

Blended systems: if the observed target is a multiple star system whose angular separation is smaller than the fibre of the RV instrument (1 arcsec for HARPS, see Mayor et al. 2003), each obtained spectrum will show the combined blended spectra of all objects. The measured RV is the flux-weighted average of all components. In Section 3.3.4, we distinguish the two scenarios, whether the brighter or fainter object are orbited by a third body.

3.3.4 *Modelling the CCFs of blended systems*

We assume a three body system in which star A is the brightest object, star B is the second star, and object C is a third body orbiting one of the stars. We assume the light from object C is negligible in comparison to stars A and B. We then can model the overall CCF extracted from a blended system as the sum of the CCF from stars A and B. As the true shapes of their CCFs are unknown, we represent them as two Gaussian functions, which is a good approximation of the true shape. The amplitudes A_A and A_B (of the Gaussians representing star A and B) depend on the product of two factors: (1) the amount of light entering the fibre from each star, F_A and F_B; 2) the intrinsic CCF contrast in dependency of the stellar spectral

type, C_A and C_B. They are directly connected to the dilution for the RV data. The dilution of stars B and A is calculated as:

$$D_{0,B}^{RV} = 1 - \frac{A_B}{A_A + A_B} = 1 - \frac{C_B F_B}{C_B F_A + C_B F_B}, \quad (3)$$

$$D_{0,A}^{RV} = 1 - D_{0,B}^{RV} \quad (4)$$

We retrieve the values for F_A and F_B from our dilution model (see Section 3.4). We further study the dependency of the contrast C_A and C_B on the stellar spectral type. Sousa et al. (2008) performed a study of 451 potential exoplanet hosts with HARPS, and estimated their effective temperatures, surface gravities, and metallicities. We retrieve the original CCFs from the HARPS archives, and extract the measured amplitudes of these targets. The CCF contrast strongly depends on the metallicity. We assume that star B has a comparable metallicity to star A, and select only objects with Fe/H between −0.03 and 0.27 (see Table 5). We further only select objects analysed with the HARPS CCF G2 mask, to be consistent with our data set. This limits the sample to stars $\gtrapprox$5000 K. We note that the contrast also strongly depends on the vsini of the star. The sample from Sousa et al. (2008) only considers vsini $\lessapprox 3\,\mathrm{km\,s^{-1}}$, and is hence biased in this regard. Due to these sample limitations, we cannot formulate an empirical relation between the CCF contrast and the stellar type for all possible parameter ranges in our global model. Therefore, we choose to instead propagate the range of possible contrast values from 40 per cent to 60 per cent as an uncertainty on to our prior for the dilution via equation (4).

Similar to the analysis by Santos et al. (2002), we use our CCF model to investigate the effect of two blend scenarios on the RV and BIS measurements in a 'toy model'. Fig. 5 displays all six simulated scenarios, which we outline in the following.

Scenarios 1–3: star B is orbited by object C: we simulate two Gaussians with $D_0^{RV} = 0.8$ and RV semi-amplitude $K_B = 2\,\mathrm{km\,s^{-1}}$. $FWHM_A$ is fixed at $7\,\mathrm{km\,s^{-1}}$, and $FWHM_B$ is varied between 6.8, 7, and $7.2\,\mathrm{km\,s^{-1}}$. We then use our BLENDFITTER toolbox to extract the RV and bisector measurements.

(1) $FWHM_B < FWHM_A$: the measured BIS is anticorrelated with the RV value. We hence caution that this scenario can mimic BIS anticorrelations introduced by atmospheric turbulence.

(2) $FWHM_B = FWHM_A$: in practice, the BIS correlation would be covered by noise and not be measurable. We hence caution that blended objects with similar FWHM can remain undetected and lead to misclassification of object C. This can lead to a wrong planet mass or false positives.

(3) $FWHM_B > FWHM_A$: the measured BIS is correlated with the RV value.

Scenarios 4–6: star A is orbited by object C: we simulate two Gaussians with $D_0^{RV} = 0.8$ and RV semi-amplitude $K_A = 0.45\,\mathrm{km\,s^{-1}}$. $FWHM_A$ is again fixed at $7\,\mathrm{km\,s^{-1}}$, and $FWHM_B$ varied between 6.8, 7, and $7.2\,\mathrm{km\,s^{-1}}$.

(4) $FWHM_B < FWHM_A$: the measured BIS is correlated with the RV value.

(5) $FWHM_B = FWHM_A$: in practice, the BIS correlation would be covered by noise and not be measurable. We hence caution that blended objects with similar FWHM can remain undetected and lead to misclassification of object C. This can lead to a wrong planet mass or false positives.

(6) $FWHM_B > FWHM_A$: the measured BIS is anticorrelated with the RV value. We hence caution that this scenario can mimic BIS anticorrelations introduced by atmospheric turbulence.

We emphasize that there is no difference between the extracted RV curves of all scenarios (Fig. 5). This underlines that including a precise bisector analysis in a global model is pivotal to minimize the false positive risk for exoplanet candidates. If a BIS correlation is detected, the signal can still originate from either star A or B. Disentangling such a system requires global analysis conjoint with multicolour information, as presented in the following. However, even in cases where no bisector correlation is detected, scenarios 2 and 5 show that a blend scenario can not be ruled out without further information.

3.3.5 *Model of the CCF FWHM of NGTS-3A and NGTS-3B*

The HARPS CCF profile's FWHM is a function of the stellar rotation and spectral type. From empirical calibrations, it can be expressed as a function of the star's $v\sin i$ and B–V colour:

$$\sigma^2 = \left(\frac{v \sin i}{1.95}\right)^2 + \sigma_0^2 \quad (5)$$

$$\sigma_0^2 = \big(8.625 - 20.037[B-V] + 23.388[B-V]^2 - 10.364[B-V]^3 + 1.273[B-V]^4\big)^2 \quad (6)$$

$$\mathrm{FWHM} = 2\sqrt{2\ln(2)\sigma^2}. \quad (7)$$

This relation is only valid for main-sequence FGK stars with effective temperatures $T_{\rm eff} \gtrapprox 3900$ K.

We next use the relations by Sekiguchi & Fukugita (2000) to relate the B–V colour to the effective temperature $T_{\rm eff}$, metallicity [Fe/H], and surface gravity log$g$.

$$\begin{aligned}[B-V] = {} & -813.3175 + 684.4585 \log T_{\rm eff} \\ & - 189.923 \log {T_{\rm eff}}^2 + 17.40875 \log {T_{\rm eff}}^3 \\ & + 1.2136[\mathrm{Fe/H}] + 0.0209[Fe/H]^2 \\ & - 0.294[\mathrm{Fe/H}] \log T_{\rm eff} - 1.166 \log g \\ & + 0.3125 \log g \log T_{\rm eff} \end{aligned} \quad (8)$$

With the values and uncertainties for star A from the spectral analysis (see Table 5), we use these relations to calculate a prior on the FWHM of star A (shown in Fig. 6a).

Next, we establish a prior on star B in dependency of $T_{\rm eff,\,B}$, which is calculated from the dilution relation (Section 3.4) and updated at each step in the MCMC. We assume that both stars formed in the same system, and hence that star B has a similar metallicity to star A. Further, as there are no signs of strong stellar line broadening, we assume that star B is a slow rotator like star A. We then evaluate the above relations for a range of $T_{\rm eff,\,B}$ from 3900 to 6000 K in steps of 1 K. Fig. 6b shows a sampling of the resulting prior on $FWHM_B$. Note the minima of the FWHM relation for early K-type stars.

3.4 Global dilution model

We assume that NGTS-3A dominates the observed light, and that the spectral analysis of the HARPS data constrains the properties of NGTS-3A. Additionally, our joint modelling of photometry and RV allows to make use of some informative priors and constraints on star B. This is incorporated in the dilution terms for stars A and

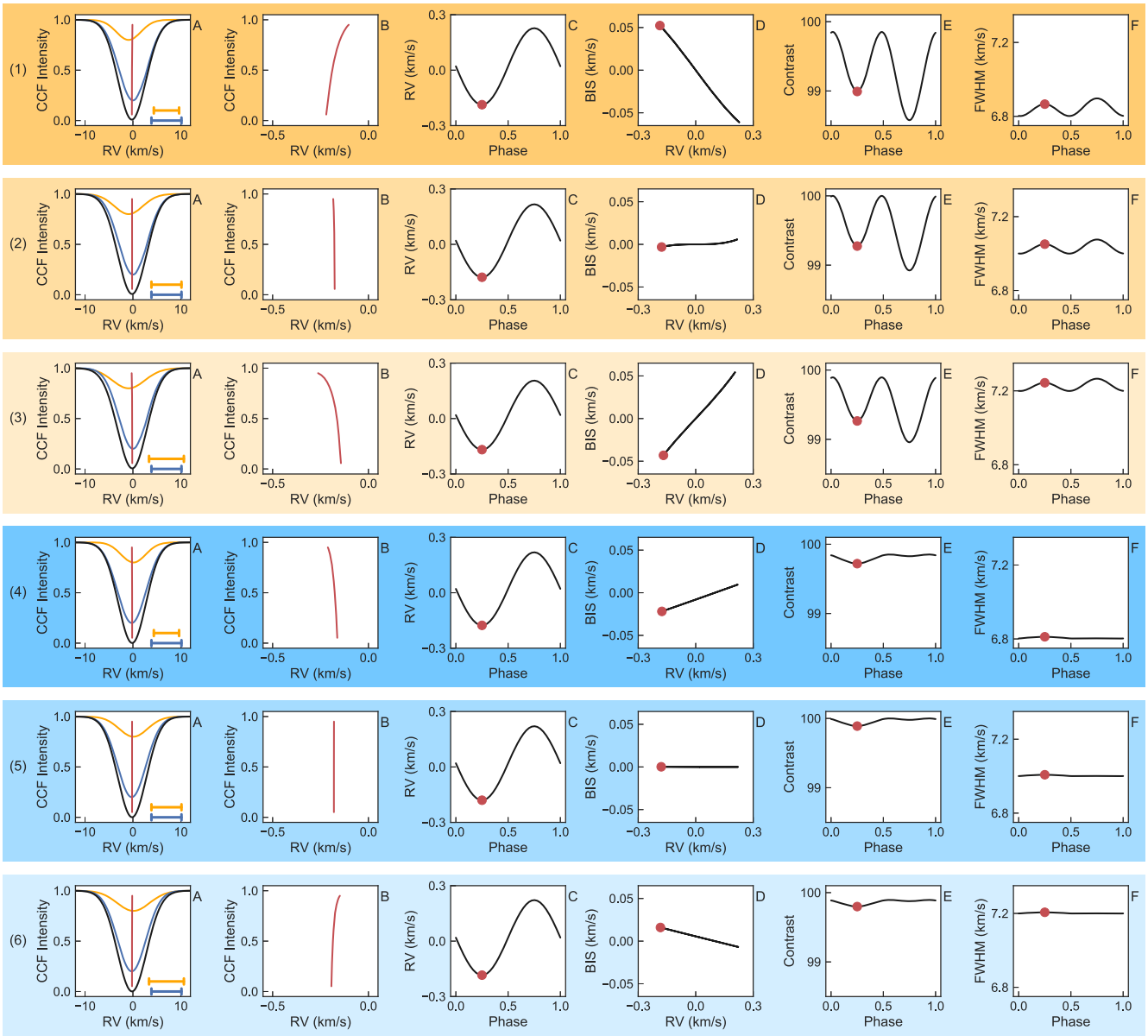

Figure 5. Example scenario of an unresolved binary system, where one star is orbited by a gas giant planet or brown dwarf. The primary was set to a systemic RV of 0 km s^{-1}, and the secondary to 0.1 km s^{-1}, reflecting the orbital motion of the two binary stars. The numbering of the scenarios refers to Section 3.3.4. The top three panels (orange background) display the scenario of a brown dwarf orbiting star B with $K = 1$ km s^{-1}. The FWHM or star B varies. First panel: $\mathrm{FWHM_B} < \mathrm{FWHM_A}$; second panel: $\mathrm{FWHM_B} = \mathrm{FWHM_A}$; and third panel: $\mathrm{FWHM_B} > \mathrm{FWHM_A}$. The bottom three panels (blue background) display the scenario of a gas giant planet orbiting star A with $K = 0.25$ km s^{-1}. The FWHM or star A varies. Fourth panel: $\mathrm{FWHM_B} < \mathrm{FWHM_A}$; fifth panel: $\mathrm{FWHM_B} = \mathrm{FWHM_A}$; and sixth panel: $\mathrm{FWHM_B} > \mathrm{FWHM_A}$. (a) Simulated CCF profile (black) and bisector (red). The profile is modelled as the sum of two Gaussian functions representing star A (blue) and star B (orange). The horizontal lines at the bottom right indicate the ratio of the FWHM. (b) Close-up of the bisector, measured from a single Gaussian fit. (c) The RV signal, measured from a single Gaussian fit, resembles a typical hot Jupiter observation in all cases. (d) The correlation of the BIS with the RV signal is a function of dilution, offset in systemic RV, and FWHM of the two stars. (e) Total CCF contrast, measured from a single Gaussian fit. (f) Total FWHM, measured from a single Gaussian fit. The red circles in (c)–(f) denote at which time the snapshot shown in (a) and (b) was taken. The offset from (0,0) in (d) and the different peak height in (e) and (f) result from the different RV zero-points of the primary and secondary. All measurements were extracted with our BLENDFITTER tools. A colour version and an animated version of this figure is available from the online journal.

B for the photometric data:

$$D_{0,\mathrm{B}}^{\mathrm{phot}} = 1 - \frac{F_\mathrm{B}}{F_\mathrm{A} + F_\mathrm{B}}, \tag{9}$$

$$D_{0,\mathrm{A}}^{\mathrm{phot}} = 1 - D_{0,\mathrm{B}}^{\mathrm{phot}}. \tag{10}$$

With the knowledge of the spectral type of NGTS-3A, we can simulate the dilution originating from different stellar companions using the telescope transmission functions and stellar model spectra. We make use of the PHOENIX stellar models (Allard & Hauschildt 1995; Husser et al. 2013). These are given in a grid, encompassing the effective temperature T_eff in steps of 100 K, $\log g$ in steps of

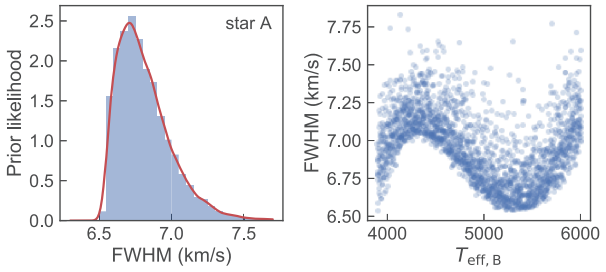

Figure 6. Prior likelihood distributions for the FWHM of (a) star A and (b) star B, the latter expressed as a function of $T_{\rm eff,\,B}$. Note the minima of the FWHM relation for early K-type stars.

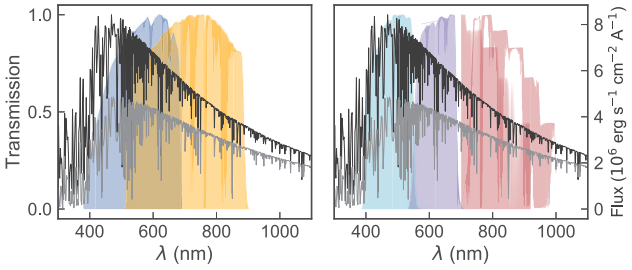

Figure 7. Dilution is a function of the instrument transmission and stellar spectral types. Left-hand axis: transmission efficiency of HARPS (blue), NGTS (orange), and the SPECULOOS *g*' band (light blue), *r*' band (purple), and *i*'+*z*' band (red), all including atmospheric absorption. Right-hand axis: luminosity of a G6V (top) and a K4V (bottom) star. The different bandpasses lead to a different dilution of the planetary signal for each instrument.

0.5, and [Fe/H] in steps of 0.5 for our range of possible properties. In practice, we employ the PYSYNPHOT software package (STScI Development Team 2013), which allows to retrieve an interpolated spectrum for any requested property.

We employ the transmission functions of the NGTS, SPECULOOS, and HARPS instruments (Wheatley et al. 2018; ESO 2011, private correspondence with the SPECULOOS consortium), which we multiply with a model of Earth's atmospheric absorption. Fig. 7 shows all resulting transmission functions, and the model spectra of a G6V and K4V dwarf overlaid as examples.

We study the dilution as a function of the spectral type of NGTS-3B. We simulate NGTS-3A with the PHOENIX model for the properties (and errors) listed in Table 5. Next, we simulate all possibilities for NGTS-3B by passing each PHOENIX model spectra in $T_{\rm eff}$ steps of 200 K through the HARPS and NGTS transmission functions. From this, we calculate the dilution of star B, $D_{0,\rm B}$, via equation (10) as a function of the effective temperature of NGTS-3B, $T_{\rm eff,\,B}$. When modelling a planet on star A, the dilution of the planet signal on star A is calculated as $D_{0,\,\rm A} = 1 - D_{0,\rm B}$. Fig. 8 shows the resulting dilution as function of $T_{\rm eff,\,B}$ for HARPS, NGTS, and all used SPECULOOS filters. We perform a fifth-order polynomial fit to all mean points and error bars. This fit can then be used to predict the dilution and its error at any chosen $T_{\rm eff,\,B}$.

3.5 Inferring properties of NGTS-3B

Without visual information on NGTS-3B, we have no a-priori knowledge of its spectral type and properties. It was not possible to constrain the spectrum of NGTS-3B from the HARPS spectra analysis (Section 3.1) nor from a spectral energy distribution (SED) fit without prior information. However, we can employ our global

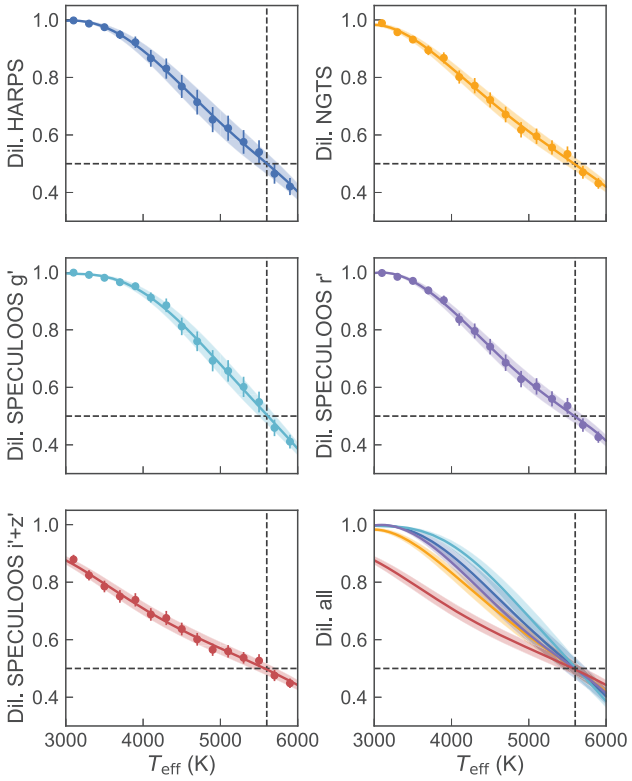

Figure 8. HARPS, NGTS, and SPECULOOS dilution of star B, $D_{0,\rm B}$, as function of its effective temperature of NGTS-3B, $T_{\rm eff,\,B}$. We derive the dilution by passing PHOENIX model spectra through the telescope bandpasses. We fit the resulting trend with a fifth-order polynomial, which can then be used to predict the dilution for each instrument at any chosen $T_{\rm eff,\,B}$. Dashed lines at dilution 0.5 and $T_{\rm eff} \approx 5600$ K indicate the properties of star A. Note that, when modelling a planet on star A, the dilution of the planet signal on star A is calculated as $D_{0,\,\rm A} = 1 - D_{0,\rm B}$.

MCMC model of the photometric and RV data to estimate the effective temperature of NGTS-3B, $T_{\rm eff,\,B}$, from our dilution model (Section 3.4). At each step in the MCMC chain of the global modelling, we sample the dilution values for all instruments. We pass them into the dilution model, allowing us to sample the likelihood distribution of $T_{\rm eff,\,B}$. We can then employ empirical relations to use $T_{\rm eff,\,B}$ for estimating the likelihood distribution of the radius $R_{\rm B}$ and mass $R_{\rm B}$ (see Sections 3.6 and 3.9). In inferring properties of NGTS-3B, we make the assumption that it is a main-sequence star. A giant star would dominate the light and would have been identified in the HARPS spectra analysis. Moreover, low-mass main-sequence stars are the most abundant objects in the night sky, and frequent companions in binary systems with a G-type primary.

3.6 Model of the RV offset between NGTS-3A and NGTS-3B

In order to model the two CCFs, the systemic RVs of NGTS-3A and NGTS-3B are needed. We will use both as free parameters to the fit in Section 3.8. However, they are tied to each other by astrophysical constraints, which we can calculate and include into our MCMC modelling.

We can calculate the RV semi-amplitude for each star, $K_{\rm A,\,B}$, in the binary system as

$$K_{\rm A,B} = \frac{M_{\rm B,A} \sin i_{\rm binary}}{(M_{\rm A} + M_{\rm B})^{2/3}} \frac{(2\pi G)^{1/3}}{P_{\rm binary}^{1/3} \left(1 - e_{\rm binary}^2\right)^{1/2}}. \quad (11)$$

Here, M_A and M_B are the masses of NGTS-3A and NGTS-3B, respectively. P_{binary}, i_{binary}, and e_{binary} are the period, inclination, and eccentricity of the binary system (not to be confused with the parameters of the planet's orbits). G is the gravitational constant.

As we have no prior knowledge about this binary system, we employ a series of empirical relations to sample the likelihood space for $K_{A,B}$ using a Monte Carlo approach. We use our result for M_A as a normal prior on this parameter (see Table 5). The inclination $i$binary is randomly drawn from a uniform distribution in cos i_{binary} between 0° and 90°. The logarithm of the period P_{binary} is randomly drawn from a normal distribution with mean 5.03 and standard deviation 2.28 (Raghavan et al. 2010). The eccentricity e_{binary} is randomly drawn from the results of Tokovinin & Kiyaeva (2016). We do not use their linear fit solution, but instead calculate an empirical cumulative distribution function (CDF) of e_{binary} from their tabulated data. We interpolate the CDF with a cubic spline function, and perform random sampling from the inverse CDF. In total, we generate 1000 random binary systems.

We then calculate the measured RV difference in dependency of the relative orbital position of the binary system, using

$$\mathrm{RV}_{A,B}(t) = K_{A,B}(\cos(\nu(t) + \omega_{A,B}) + \mathrm{e}\cos(\nu(t))), \quad (12)$$

$$\Delta\mathrm{RV}(t) = |\mathrm{RV}_A(t) - \mathrm{RV}_B(t)|\,. \quad (13)$$

Here, ΔRV denotes the difference in systemic RV that we expect between the two stars, which is the direct result of their gravitational pull on each other. ν is the true anomaly of the system, and $\omega_{A,B}$ the argument of periastron with $\omega_B = \omega_A - 180$ deg.

The parameter ω_A is sampled from a uniform distribution between 0° and 360°. For each system, we compute ν as a function of time. This is done by calculating the mean anomaly, and then solving Kepler's equation for the eccentric anomaly. Finally, ν is computed from the eccentric anomaly. We evaluate ν for 100 uniformly spaced times in the range from 0 to P_{binary}, sampling the entire orbit for each system.

By combining all this in equation (13), we derive ΔRV as a function of the unknown mass of NGTS-3B. Fig. 9a shows the distribution of ΔRV on the example for all simulated distributions of binary systems with a G6V primary and K1V secondary. To generate priors for our global MCMC fit, we evaluate equation (13) for 100 different probe masses for star B, uniformly spaced in the range 0.1–1 $M_\odot$. This means we have a total of 1000 binaries × 100 time points × 100 probe masses = 10^7 samples.

We next link mass to effective temperature using the empirical catalogue of mean dwarf stars by Pecaut & Mamajek (2013). This mean dwarf model is chosen to rely on as little prior assumptions as possible for the global MCMC fit, as we initially had no information on the spectral type of NGTS-3B. It relies only on the assumption that NGTS-3B is a main-sequence star (see Section 3.5). We use GP regression with an squared exponential kernel[4] and a constant kernel to fit the data in Pecaut & Mamajek (2013):

$$k\left(r^2\right) = c\mathrm{e}^{-\sqrt{r^2}} \quad (14)$$

(for discussion of the GP fitting procedure, see Section 3.3.1). The resulting fit is then used to predict $T_{eff,B}$ for any requested M_B, translating the prior on ΔRV to be a function of $T_{eff,B}$. Its value is calculated at each step in the MCMC chain as described in Section 3.5.

[4]Also referred to as 'exponentiated quadratic kernel'.

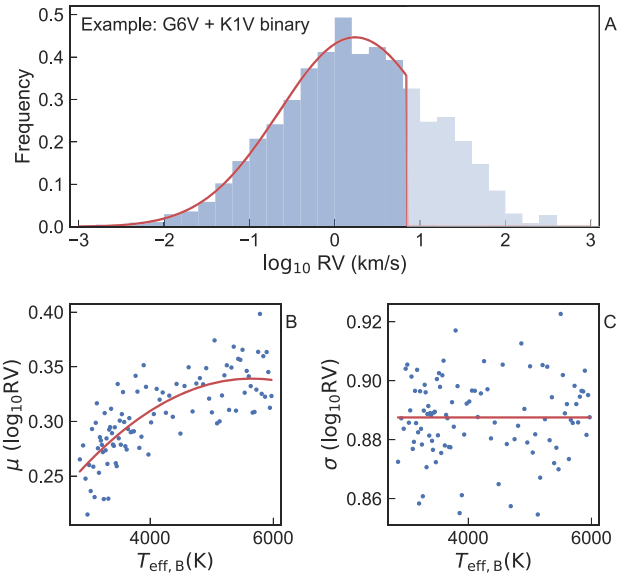

Figure 9. (a) RV difference between the two stars of a G6V–K1V binary system from 1000 simulations and sampled at 100 points in phase. The truncation is set by the fact that both systems remain unresolved in HARPS. Hence, their separation has to be $\lesssim$7 km s^{-1}, given by the measured FWHM. The red curve shows a truncated Gaussian fit to the logarithm of the measured RV differences. We fix star A to the properties of NGTS-3A and simulate 1000 binary systems for M_B ranging from 0.1 to 1 $M_\odot$ in steps of 0.01 $M_\odot$. We sample each system at 100 points in phase. We calculate $T_{eff,B}$ from M_B, using our empirical relation described in Section 3.5. We then calculate the (b) mean and (c) standard deviation of the Gaussian fit to log ΔRV for all sampled $T_{eff,B}$. Red curves in (b) and (c) show a second-order polynomial (constant) fit to the mean (standard deviation) as a function of $T_{eff,B}$.

Next, we fit the resulting logarithmic distribution of ΔRV with a Gaussian function. When studying the mean $\mu(\log_{10}\Delta\mathrm{RV})$ and standard deviation $\sigma(\log_{10}\Delta\mathrm{RV})$ of this Gaussian function in dependency of $T_{eff,B}$, we find a clear trend (Figs 9b and c). We describe $\mu(\log_{10}\Delta\mathrm{RV})$ with a second-order polynomial and $\sigma(\log_{10}\Delta\mathrm{RV})$ by its mean value. We substitute $x = (T_{eff,B} - 3000\mathrm{K})/3000$ K, and find the following relations:

$$\mu\,(\log\Delta\mathrm{RV}) = -0.144x^2 + 0.212x + 0.262 \quad (15)$$

$$\sigma\,(\log\Delta\mathrm{RV}) = 0.887. \quad (16)$$

These equations are then used in our MCMC model (Section 3.8) to constrain the systemic velocities in relation to each other for any evaluated $T_{eff,B}$. Additionally, an upper limit on ΔRV is set by the fact that both systems remain unresolved in HARPS. Hence, their separation has to be $\lesssim$7 km s^{-1}, constrained by the measured FWHM. We hence implement a truncated Gaussian prior on ΔRV as a function of $T_{eff,B}$.

3.7 Detrending NGTS' photometric and centroid data with Gaussian process regression

To decrease the influence of systematic noise, we pre-whiten the photometric and centroid data from NGTS. We first mask all data during primary and secondary eclipses. We then employ a GP regression fit using the product of a Matern 3/2 kernel and a constant kernel (see also Section 3.3.1). We detrend the light and centroid curves with the resulting GP.

Table 7. Priors for the global MCMC model. Parameters are described in Table 9.

Δx	$\mathcal{U}(-0.2, 0.2)$ pixel
Δy	$\mathcal{U}(-0.2, 0.2)$ pixel
$D_{0,\,A}$ for each instrument	see Section 3.4; in (0,0.5)
P	$\mathcal{U}(0, 10^{12})$ min
$T_0 - 2450000\,d$	$\mathcal{U}(0, 10^{12})$ min
R_p/R_A	$\mathcal{U}(0, 1)$
$(R_A + R_p)/a$	$\mathcal{U}(0, 1)$
$\cos i$	$\mathcal{U}(0, 1)$
$RV_{sys,\,A}$	see Section 3.6; in (0,100) km s^{-1}
$RV_{sys,\,B}$	see Section 3.6; in (0,100) km s^{-1}
K	$\mathcal{U}(-100, 100)$ km s^{-1}
A_{CCF}	$\mathcal{U}(0, 1)$
$FWHM_{CCF,\,A}$	$\mathcal{U}(0, 100)$ km s^{-1}
$FWHM_{CCF,\,B}$	$\mathcal{U}(0, 100)$ km s^{-1}
All photometric errors	$\mathcal{U}(0, 1000)$ mmag
All centroid errors	$\mathcal{U}(0, 1000)$ mpixel
RV and BIS errors	$\mathcal{U}(0, 1)$ km s^{-1}
FWHM error	$\mathcal{U}(0, 10)$ km s^{-1}
Contrast error	$\mathcal{U}(0, 1)$
CCF errors	$\mathcal{U}(0, 10)$

3.8 Global MCMC model

We perform a global, joint MCMC modelling of all data sets: the GP detrended photometric and centroid data from NGTS, the HARPS CCFs for the seven exposures, and the extracted HARPS RV and bisector measurements.

Priors: in multiple initial MCMC test runs, we explore the scenario of a planet or sub-stellar object orbiting either star A or B. We also explore the parameter space from different starting points, with different priors and more free parameters. We find that all approaches converge to the scenario of a planet orbiting star A. From our previous analyses (Sections 3.1–3.6), we can hence put various priors and constraints (Table 7; see Table 9 for a description of the parameters):

(i) An upper limit of 1 arcsec projected separation between NGTS-3A and NGTS-3B (acceptance of the HARPS fibre) as a uniform, informative prior constraining the centroid model. One NGTS pixel spans 4.97 arcsec, leading to limits of $\Delta x \in (-0.2, 0.2)$ pixel and $\Delta y \in (-0.2, 0.2)$ pixel.

(ii) The dilution relation from Section 3.4, linking the different instruments. As we model the scenario of a planet on star A (constrained by the colour difference in transit depth), we restrict the dilution further to $D_{0,\,A} \in (0, 0.5)$.

(iii) The RV offset relation from Section 3.6.

(iv) Uniform priors on all other parameters, where applicable within physical bounds, otherwise with non-restrictive bounds.

We note that all our priors are jointly proper, ensuring posterior propriety. None of our priors are unbounded, and the likelihood functions for all models converge to 0 as the model deviates from the data.

Fixed values: we fix the eccentricity to $e = 0$, as there is no evidence for eccentricity from the HARPS RV data (see e.g. discussion in Anderson et al. 2012). The surface brightness ratio, gravitational darkening and reflectivity are also fixed to 0, following a planet scenario. For each bandpass, we compute quadratic limb darkening parameters for star A from the values in Table 5 using the open-source code by Espinoza & Jordán (2015) and the PHOENIX model spectra (Husser et al. 2013). To reduce free parameters in our model, we fix the limb darkening parameters α and β to the values shown in Table 8.

Table 8. Limb darkening parameters for the global MCMC model.

	α	β
NGTS	0.4294	0.2019
SPEC. *g*'	0.6993	0.0946
SPEC. *r*'	0.4869	0.1927
SPEC. *i*'+*z*'	0.3339	0.2199

Baselines: from our re-analysis of the HARPS CCFs in Section 3.3.1, we find that for all studied CCFs our GP model favours a simple and continuous baseline trend, which can be closely reproduced by a low-order polynomial baseline. To minimize the complexity and number of dimensions of our MCMC model, we therefore opt to use polynomial baselines instead of GPs in the global modelling. In particular, we allow a fourth-order polynomial for the baseline of the HARPS CCFs, and a second-order polynomial for the baseline of the SPECULOOS data. As the NGTS data cover mostly out-of-transit data, we remove any global variation using a GP regression fit beforehand (see Section 3.7), and include only a constant baseline for any NGTS data in our global model. In fitting the baseline polynomials, we do not implement the polynomial values as jump parameters in our MCMC, but instead perform an algebraic least-squares fit to the residuals of each MCMC fit at each step in the MCMC chain. This approach was proven robust and effective in multiple previous studies (see e.g. Gillon et al. 2012).

MCMC: the MCMC is implemented using EMCEE (Foreman-Mackey et al. 2013) and the EB binary star model (Irwin et al. 2011). We run our MCMC analysis on 37 dimensions with 500 walkers for 200 000 total steps. 19 of these dimensions are scaling factors for the errors of each data set. Across all chains, we find a median (maximal) autocorrelation length of 2,400 ($\sim$3, 400) steps. The total chain is $\sim$83 ($\sim$59) times its median (maximal) autocorrelation length, which is considered as sufficient for convergence. We discard the first $\sim$50 000 steps as burn-in phase, and thin the chain by a factor of 2500. This results in $(200,000-50\,000)/2\,500 * 500 = 30\,000$ independent samples.

Results: the hot Jupiter NGTS-3Ab is orbiting NGTS-3A with a period of 1.675 d. The planet radius and mass are $R_{planet} = 1.48 \pm 0.37$ R$_J$ and $M_{planet} = 2.38 \pm 0.26$ M$_J$, conform with a potentially inflated gas giant planet. We find a dilution of 0.38–0.43 of the transit signal, depending on the instrument bandpass. NGTS-3Ab has an undiluted transit depth of $\delta_{undil.} = (R_{planet}/R_A)^2 = 2.68 \pm 0.15$ per cent. The planet introduces an undiluted RV signal of $K = -0.404 \pm 0.035$ km s^{-1} on NGTS-3A. The systemic velocities of NGTS-3A and B are $RV_{sys,\,A} = 8.566 \pm 0.049$ km s^{-1} and $RV_{sys,B} = 9.032^{+0.085}_{-0.064}$ km s^{-1}, respectively. All results of our MCMC analysis can be found in Figs 1 and 10, and Table 9.

3.9 Identifying NGTS-3B

Using the approach outlined in Section 3.5, we estimate the effective temperature of NGTS-3B from the dilution model, and find $T_{eff,B} = 5230^{+190}_{-220}$ K. This places NGTS-3B most likely as an K1V dwarf (ranging G9V–K2V; see e.g. Pecaut & Mamajek 2013). From this, we calculate the final radius and mass of NGTS-3B, but deviate here from Section 3.6. The approach in Section 3.6 was chosen to find the mass for mean dwarf stars in dependency of $T_{eff,\,B}$ as we had no prior information on NGTS-3B. This does not allow to

Table 9. Parameters of the NGTS-3 system. Values and error bars are the median and 16th/84th percentile of the MCMC posterior likelihood distributions.

	Fitted parameters (astrophysical)		
Δx	Relative CCD x position of the blend	85^{+72}_{-87}	mpixel
Δy	Relative CCD y position of the blend	133^{+47}_{-71}	mpixel
$D_{0,\,\mathrm{A,\,NGTS}}$	Dilution of star A in NGTS	$0.434^{+0.030}_{-0.032}$	
$D_{0,\mathrm{A,SPEC.g'}}$	Dilution of star A in SPECULOOS g' band	$0.409^{+0.035}_{-0.038}$	
$D_{0,\mathrm{A,SPEC.r'}}$	Dilution of star A in SPECULOOS r' band	$0.432^{+0.031}_{-0.034}$	
$D_{0,\mathrm{A,SPEC.i'+z'}}$	Dilution of star A in SPECULOOS i'+z' band	0.449 ± 0.027	
$D_{0,\,\mathrm{A,\,HARPS}}$	Dilution of star A in HARPS	$0.424^{+0.045}_{-0.051}$	
P	Period	1.6753728 ± 0.0000030	d
T_0	Epoch (HJD–2450000)	7620.16790 ± 0.00095	d
$R_{\mathrm{planet}}/R_{\mathrm{A}}$	Ratio of radii	0.1638 ± 0.0045	
$(R_{\mathrm{A}} + R_{\mathrm{planet}})/a$	Sum of radii over the semimajor axis of the planet's orbit	$0.1792^{+0.0012}_{-0.0011}$	
$\cos i$	Cosine of the inclination	$0.0077^{+0.0085}_{-0.0054}$	
$\mathrm{RV}_{\mathrm{sys,\,A}}$	Systemic RV of NGTS-3A	8.566 ± 0.049	km s^{-1}
$\mathrm{RV}_{\mathrm{sys,\,B}}$	Systemic RV of NGTS-3B	$9.032^{+0.085}_{-0.064}$	km s^{-1}
K	RV semi-amplitude	-0.404 ± 0.035	km s^{-1}
	Fitted parameters (other)		
A_{CCF}	Maximal amplitude of the CCF profile	$0.52147^{+0.00076}_{-0.00070}$	
$\mathrm{FWHM}_{\mathrm{CCF,\,A}}$	FWHM of the CCF profile of NGTS-3A	7.436 ± 0.082	km s^{-1}
$\mathrm{FWHM}_{\mathrm{CCF,\,B}}$	FWHM of the CCF profile of NGTS-3B	$6.857^{+0.078}_{-0.090}$	km s^{-1}
$\sigma(F_{\mathrm{NGTS}})$	Error of the flux in NGTS	10.247 ± 0.079	mmag
$\sigma(\xi_x)$	Error of the centroid in x	12.114 ± 0.097	mpixel
$\sigma(\xi_x)$	Error of the centroid in y	11.926 ± 0.095	mpixel
$\sigma(F_{\mathrm{SPEC.Callisto,g'}})$	Error of the flux in SPEC. Callisto g' band	$2.846^{+0.099}_{-0.093}$	mmag
$\sigma(F_{\mathrm{SPEC.Callisto,r'}})$	Error of the flux in SPEC. Callisto r' band	$3.03^{+0.13}_{-0.12}$	mmag
$\sigma(F_{\mathrm{SPEC.Europa,r'}})$	Error of the flux in SPEC. Europa r' band	$2.597^{+0.087}_{-0.082}$	mmag
$\sigma(F_{\mathrm{SPEC.Europa,i'+z'}})$	Error of the flux in SPEC. Europa i'+z' band	$2.512^{+0.085}_{-0.080}$	mmag
$\sigma(F_{\mathrm{SPEC.Io,i'+z'}})$	Error of the flux in SPEC. Io i'+z' band	2.517 ± 0.084	mmag
σ(RV)	Error of the RV	$0.043^{+0.017}_{-0.010}$	km s^{-1}
σ(BIS)	Error of the BIS	$0.0317^{+0.015}_{-0.0097}$	km s^{-1}
σ(FWHM)	Error of the FWHM	$0.084^{+0.037}_{-0.023}$	km s^{-1}
σ(contrast)	Error of the contrast	$1.61^{+0.66}_{-0.41}$	
σ(CCF)	Error of the CCF 1	$0.00322^{+0.00019}_{-0.00018}$	
σ(CCF)	Error of the CCF 2	$0.00611^{+0.00036}_{-0.00033}$	
σ(CCF)	Error of the CCF 3	$0.00574^{+0.00035}_{-0.00031}$	
σ(CCF)	Error of the CCF 4	$0.00397^{+0.00025}_{-0.00022}$	
σ(CCF)	Error of the CCF 5	$0.00436^{+0.00026}_{-0.00024}$	
σ(CCF)	Error of the CCF 6	$0.00484^{+0.00030}_{-0.00027}$	
σ(CCF)	Error of the CCF 7	$0.00518^{+0.00030}_{-0.00028}$	
	Derived parameters for NGTS-3B		
$T_{\mathrm{eff,\,B}}$	Effective temperature of NGTS-3B	5230^{+190}_{-220}	K
R_{B}	Radius of NGTS-3B	$0.77^{+0.22}_{-0.16}$	$\mathrm{R}_\odot$
M_{B}	Mass of NGTS-3B	$0.88^{+0.14}_{-0.12}$	$\mathrm{M}_\odot$
ρ_{B}	Density of NGTS-3B	$1.13^{+0.29}_{-0.23}$	$\rho_\odot$
	Derived parameters for NGTS-3Ab		
R_{planet}	Radius of the planet	1.48 ± 0.37	$\mathrm{R_J}$
M_{planet}	Mass of the planet	2.38 ± 0.26	$\mathrm{M_J}$
ρ_{planet}	Density of the planet	$0.31^{+0.41}_{-0.15}$	ρ_{J}

Table 9 – *continued*

Fitted parameters (astrophysical)			
i	Inclination	$89.56^{+0.31}_{-0.48}$	deg
$R_{\rm planet}/a$	Planet radius over semimajor axis of the planet's orbit	0.02523 ± 0.00071	
$R_{\rm A}/a$	Radius of NGTS-3A over semimajor axis of the planet's orbit	$0.15398^{+0.00082}_{-0.00069}$	
a	Semimajor axis of the planet's orbit	$5.0^{+1.4}_{-1.0}$	$R_\odot$
$T_{1\text{-}4}$	Total duration of transit	138.15 ± 0.82	min
$T_{2\text{-}3}$	Transit width	98.82 ± 0.63	min
$\delta_{\rm undil.} = (R_{\rm planet}/R_{\rm A})^2$	Undiluted (real) depth of the transit	2.68 ± 0.15	per cent
$b_{\rm tra}$	Impact parameter of the transit	$0.050^{+0.055}_{-0.035}$	
Derived parameters for the NGTS-3 binary system			
$\Delta x_{\rm sky}$	Relative sky position of the blend in x	$0.42^{+0.36}_{-0.43}$	arcsec
$\Delta y_{\rm sky}$	Relative sky position of the blend in y	$0.66^{+0.23}_{-0.35}$	arcsec
d	Distance to the system	1010^{+150}_{-130}	pc
$a_{\rm binary}$	Orbital separation between the stars	>500	au
$P_{\rm binary}$	Orbital period of the binary stars	>11000	yr

estimate uncertainties, particularly it is not possible to propagate uncertainties on $\log g_{\rm B}$ and $[{\rm Fe/H}]_{\rm B}$.

For the calculation of uncertainties, we here estimate $R_{\rm B}$ and $M_{\rm B}$ from $T_{\rm eff,\,B}$ by using the empirical relations by Torres, Andersen & Giménez (2010a). These relations depend on $T_{\rm eff,\,B}$, $\log g_{\rm B}$, and $[{\rm Fe/H}]_{\rm B}$. We estimate a prior on $\log g_{\rm B} \in \mathcal{N}(4.6, 0.2)$ using the data by Pecaut & Mamajek (2013) for our result $T_{\rm eff,B} = 5230^{+190}_{-220}$ K. We further assume that NGTS-3A and B formed in the same system, and hence show similar metallicity. We hence set a metallicity prior of $[{\rm Fe/H}]_{\rm B} \in \mathcal{N}(0., 0.5)$.

We find that $R_{\rm B} = 0.77^{+0.22}_{-0.16}$ $R_\odot$ and $M_{\rm B} = 0.88^{+0.14}_{-0.12}$ $M_\odot$. Table 9 summarizes all inferred results. Fig. 11 shows the inferred distributions for all parameters.

3.10 Identifying NGTS-3Ab

We use the MCMC chains and our inference of the systems dilution to calculate the properties of NGTS-3Ab, the object orbiting NGTS-3A. We can estimate the radius of NGTS-3Ab directly from the MCMC samples of the ratio of radii, $R_{\rm C}/R_{\rm A}$, and the prior on $R_{\rm A}$. We find $R_{\rm planet} = 1.48 \pm 0.37$. We estimate the mass of NGTS-3Ab with the binary mass function f for spectroscopic single-lined binaries:

$$f := \frac{PK^3(1-{\rm e}^2)^{\frac{3}{2}}}{2\pi G} = \frac{M_{\rm C}^3 \sin i^3}{(M_{\rm C}+M_{\rm A})^2} \tag{17}$$

We solve this equation for all MCMC samples (P, K, i) and the prior on $M_{\rm A}$. We find $M_{\rm planet} = 2.38 \pm 0.26$. Table 9 summarizes all derived results. Fig. 11 shows the inferred distributions for all parameters.

3.11 Identifying the binary orbit

We find a significant difference in systemic RV for NGTS-3A and B (Table 9), but it is not straightforward to use this to constrain the orbital separation; the likelihood space for ΔRV spans orders of magnitudes and depends on its orbital parameters, which remain unconstrained (see Section 3.6). However, we can use the centroid information to constrain the projected separation. With an estimate of the distance to the system, this can be translated into an orbital separation.

We perform an SED fit to the magnitudes reported in Table 5 following the method presented in Gillen et al. (2017). For modelling of the two stars NGTS-3A and NGTS-3B, we use two separate stellar model spectra from PHOENIX. As priors, we use our results of the spectral analysis for NGTS-3A ($R_{\rm A}$, $T_{\rm eff,\,A}$, $\log g_{\rm A}$; see Table 5), and the inferred posterior likelihoods for NGTS-3B ($R_{\rm B}$, $T_{\rm eff,\,B}$; see Table 9). The prior on the surface gravity is again chosen to be $\log g_{\rm B} \in \mathcal{N}(4.6, 0.2)$ (see Section 3.9). We here fix $[{\rm Fe/H}]_{\rm A,\,B} = 0$ to avoid interpolation over wide ranges of metallicity (the PHOENIX spectra are given in steps of 0.5 in metallicity). We find a distance of $d = 1010^{+150}_{-130}$ pc to the binary system.

Using this result, we can translate the projected sky separation of $\Delta x_{\rm sky} = 0.42^{+0.36}_{-0.43}$ arcsec and $\Delta y_{\rm sky} = 0.66^{+0.23}_{-0.35}$ arcsec (constrained by the centroid data in our global MCMC model; see Table 9) into au. This gives a lower limit on the orbital semimajor axis of the binary, which is $a_{\rm binary} > 500$ au. Using Kepler's third law, we can determine that the binary period is $P_{\rm binary} > 11000$ yr . At this orbital separation, we do not expect to detect any transit-timing variations (TTVs). Indeed, there was no evidence for any TTVs in the data. The resulting binary orbit agrees well with typical scenarios of a planet in a binary system, further supporting the evidence for NGTS-3Ab.

4 DISCUSSION

4.1 NGTS-3 as a cautionary tale of careful vetting

Only careful modelling of multicolour photometry, centroids and RV CCF profiles, and their bisectors enabled the verification of NGTS-3Ab. From single-colour photometry, centroids, and RV measurements alone, NGTS-3Ab would have been misclassified as an undiluted hot Jupiter orbiting an isolated G-type star.

On the other hand, a simpler consideration of the bisector correlation would have led to it being rejected as a planet. This finding is important to consider, as the bisector correlation is a common planet vetting criteria. It might have previously led to the erroneous rejection of bona-fide planets in unresolved binary systems.

We particularly raise caution that single-colour photometry alone, even if combined with precision centroiding, was not sufficient to

identify the three-body nature of this system. Only if combined with multicolour information and an analysis of the RV CCF profiles and BIS measurements, we were able to unmask the hidden nature of this system.

We caution that scenarios like NGTS-3 might be more common than currently anticipated. Unresolved companions dilute exoplanet transit signals, biasing measured planetary quantities and potentially leading to misclassification. Diluted gas giant planets or Brown Dwarf companions in unresolved binary systems can also mimic Neptune-sized and rocky exoplanets.

NGTS-3 is not resolved in Gaia DR2, which was released during revision of this publication and is complete to an angular resolution of 0.4–0.5 arcsec separation (Gaia Collaboration et al. 2018). The non-identification of the companion in Gaia DR2 is in agreement with the results of our global MCMC model, predicting a separation around the completeness limit of Gaia DR2 (see Table 9). This highlights that hidden companion stars to exoplanet hosts in multistar systems can remain unresolved in Gaia DR2. Moreover, there was no sign of the companion in the SPECULOOS images, nor the HARPS guider images. It is hence crucial for transit surveys like NGTS and the upcoming TESS mission to account for the resolution limits of follow-up instruments and catalogues like Gaia DR2.

The most robust way to identify hidden systems is a systematic lucky imaging or adaptive optics follow-up. Ideally, this would be conducted for any exoplanet system. In the case of NGTS-3, this

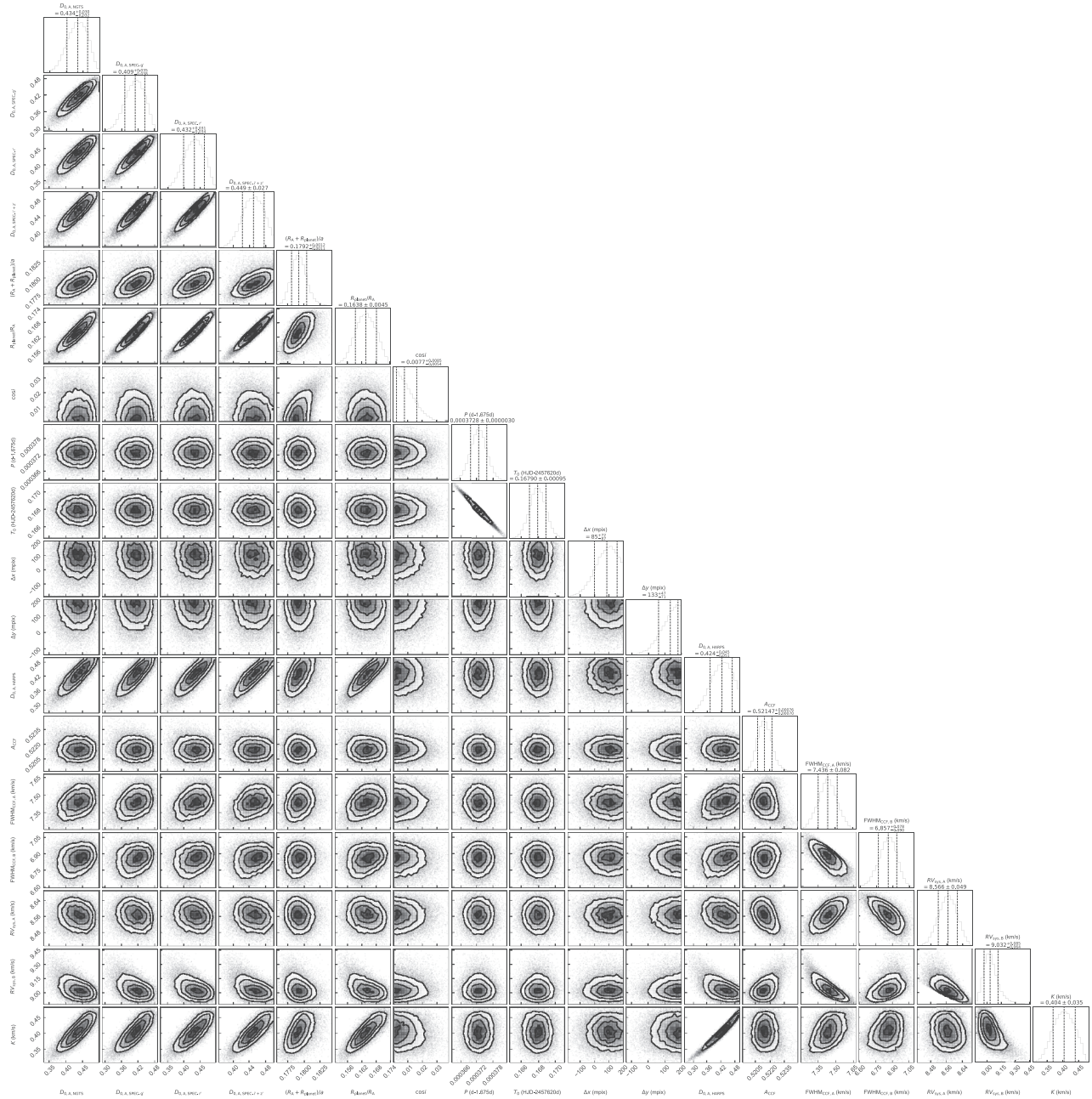

Figure 10. Posterior likelihood distributions for all astrophysical parameters of the MCMC fit to NGTS-3. For better visibility, the error scaling parameters are not shown here. Parameters are described in Table 9.

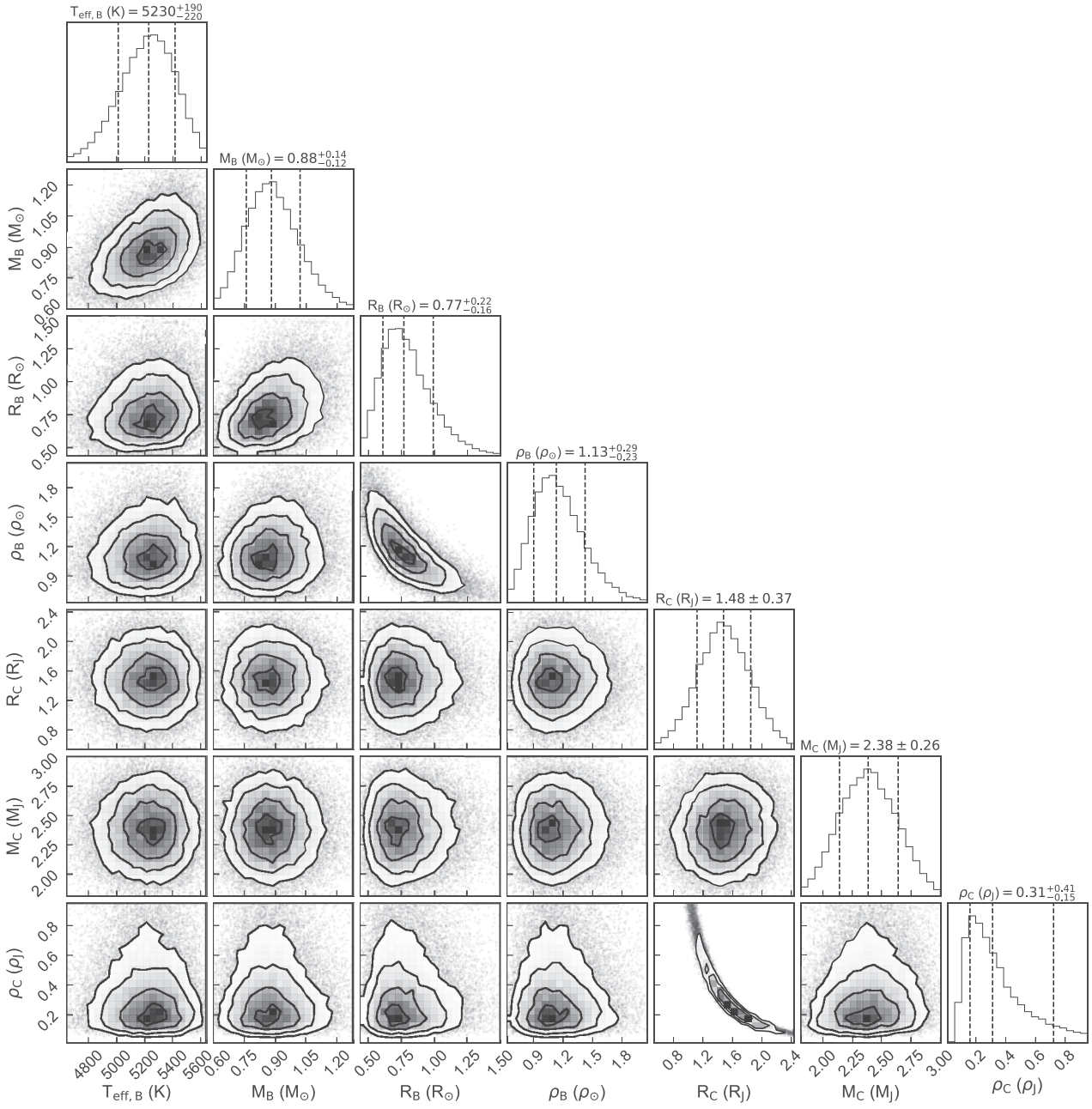

Figure 11. Likelihood distributions for the derived parameters for NGTS-3B and NGTS-3Ab, as inferred from the results of our MCMC fit. Parameters are described in Table 9.

will also allow to verify the accuracy of our modelling. We therefore aim to propose for high-resolution imaging of NGTS-3. Exploring this system further will place constraints on its binary companions, consequently refining the planetary parameters.

4.2 Caveats and prospects

4.2.1 Priors on stars A and B

We draw our priors on star A from the HARPS spectral analysis. We caution that this is only correct if the flux from star A dominates the spectrum. In the case of similar luminosity of stars A and B, the spectrum will be significantly influenced by both stars. The spectral analysis then approximately reflects a mean value between the two stars. As our findings indicate that star B contributes to the overall spectrum, we might underestimate the effective temperature of star A.

Due to lack of any knowledge of star B, we have to assume it is a slow-rotating main-sequence star, which has the same prior on its metallicity as star A. While reasonable, this assumption might cause a slight bias.

4.2.2 Calibration of the HARPS CCF G2 mask

There is no calibration of the HAPRS CCF G2 mask covering the entire range of effective temperatures from 3000 to 6000 K. In

particular, the model will profit from the following two calibrations:

$$\text{Contrast} = f\,(T_{\rm eff}, \log g, [\text{Fe/H}])\,, \tag{18}$$

$$\text{FWHM} = f\,(T_{\rm eff}, \log g, [\text{Fe/H}])\,. \tag{19}$$

In Section 3.3.4, we studied these relations. While the current HARPS calibrations allow to constrain the relationship for the FWHM for effective temperatures $\gtrsim$3900 K, there is no such calibration for the contrast. Our analysis of data from Sousa et al. (2008) only allowed to constrain the contrast for effective temperatures $\gtrsim$5000 K. To avoid introducing a bias into the fit due to the break at this temperature, we decided to use uniform priors instead (which, however, by itself introduces some bias).

5 CONCLUSION

We report the disentanglement of a previously unresolved three-body system, NGTS-3, from multicolour photometry, centroiding and RV cross-correlation profiles. We highlight the discovery of NGTS-3Ab, a potentially inflated hot Jupiter ($R_{\rm planet} = 1.48 \pm 0.37$ R_J and $M_{\rm planet} = 2.38 \pm 0.26$ M_J) in a 1.675 d orbit around the primary of an unresolved binary system. This provides an interesting test bed for planet formation, migration and orbital stability, as well as stellar multiplicity and metallicity.

Binary and triple systems are numerous. They frequently mimic exoplanet signals in photometric and RV observations. We develop a thorough analysis framework, packaged in our BLENDFITTER tool, to unmask such false positives and identify the true cause of detected signals. In particular, we analyse the photometric flux centroid as well as the RV CCFs and their bisectors.

ACKNOWLEDGEMENTS

This research is based on data collected under the NGTS project at the ESO La Silla Paranal Observatory. NGTS is operated with support from the UK Science and Technology Facilities Council (STFC; project reference ST/M001962/1). Construction of the NGTS facility was funded by the University of Warwick, the University of Leicester, Queen's University Belfast, the University of Geneva, the Deutsches Zentrum für Luft- und Raumfahrt e.V. (DLR; under the 'Großinvestition GI-NGTS'), the University of Cambridge, and STFC. The research leading to these results has received funding from the European Research Council under the FP/2007-2013 ERC Grant agreement numbers 336480 (SPECULOOS) and 320964 (WDTracer), and from the ARC grant for Concerted Research Actions, financed by the Wallonia-Brussels Federation. This work was also partially supported by a grant from the Simons Foundation (PI: Queloz, grant number 327127). This work has further made use of data from the European Space Agency (ESA) mission *Gaia* (https://www.cosmos.esa.int/gaia), processed by the Gaia Data Processing and Analysis Consortium (DPAC, https://www.cosmos.esa.int/web/gaia/dpac/consortium). Funding for the DPAC has been provided by national institutions, in particular the institutions participating in the Gaia Multilateral Agreement. Moreover, this publication makes use of data products from the 2MASS, which is a joint project of the University of Massachusetts and the Infrared Processing and Analysis Center/California Institute of Technology, funded by the National Aeronautics and Space Administration and the National Science Foundation. We make use of PYTHON programming language (Rossum 1995) and the open-source PYTHON packages NUMPY (van der Walt, Colbert & Varoquaux 2011), SCIPY (Jones et al. 2001), MATPLOTLIB (Hunter 2007), PANDAS (McKinney 2010), EMCEE (Foreman-Mackey et al. 2013), GEORGE (Ambikasaran et al. 2016), CORNER (Foreman-Mackey 2016), SEABORN (https://seaborn.pydata.org/index.html), PYASTRONOMY (https://github.com/sczesla/PyAstronomy), and PYSYNPHOT (STScI Development Team 2013),

IRAFIRAFEBOPJKTEBOPLIMB-DARKENING (Espinoza & Jordán 2015), and EB (Irwin et al. 2011). The latter is based on the previous (Southworth, Maxted & Smalley 2004a; Southworth et al. 2004b) and codes (Popper & Etzel 1981), and models by Etzel (1981), Mandel & Agol (2002), Binnendijk (1974a,b), and Milne (1926). We also make use of . is distributed by the National Optical Astronomy Observatory, which is operated by the Association of Universities for Research in Astronomy, Inc., under cooperative agreement with the National Science Foundation. MNG is supported by the UK STFC award reference 1490409 as well as the Isaac Newton Studentship. LD acknowledges support from the Gruber Foundation Fellowship. DJA, TL, DP, RGW, and PJW are supported by an STFC consolidated grant (ST/P000495/1). MG is FNRS-F.R.S. Research Associate. EJ is a senior research scientist at the Belgian FNRS. MRG and MB are supported by an STFC consolidated grant (ST/N000757/1).

REFERENCES

Allard F., Hauschildt P. H., 1995, ApJ, 445, 433
Almenara J. M. et al., 2009, A&A, 506, 337
Ambikasaran S., Foreman-Mackey D., Greengard L., Hogg D. W., O'Neil M., 2016, TPAMI, 38, 2, 252–265
Anderson D. R. et al., 2012, MNRAS, 422, 1988
Batalha N. M. et al., 2010, ApJ, 713, L103
Binnendijk L., 1974a, Vistas Astron., 16, 61
Binnendijk L., 1974b, Vistas in Astron., 16, 85
Boisse I., Bouchy F., Hébrard G., Bonfils X., Santos N., Vauclair S., 2011, A&A, 528, A4
Burdanov A., Delrez L., Gillon M., Jehin E., Speculoos T. Trappist Teams 2017, in Deeg H. J., Belmonte J. A., eds, SPECULOOS Exoplanet Search and Its Prototype on TRAPPIST, Handbook of Exoplanets. Springer-Verlag, Berlin, p. 130
Cameron A. C., 2012, Nature, 492, 48
Coughlin J. L. et al., 2016, ApJS, 224, 12
Díaz R. F., Almenara J. M., Santerne A., Moutou C., Lethuillier A., Deleuil M., 2014, MNRAS, 441, 983
Doyle A. P. et al., 2013, MNRAS, 428, 3164
Doyle A. P., Davies G. R., Smalley B., Chaplin W. J., Elsworth Y., 2014, MNRAS, 444, 3592
ESO 2011, Technical Report 3P6-MAN-ESO-90100-0005, HARPS User Manual 2.1, ESO
Espinoza N., Jordán A., 2015, MNRAS, 450, 1879
Etzel P. B., 1981, in Carling E. B., Kopal Z., eds, Photometric and Spectroscopic Binary Systems. D. Reidel Publishing Co., Dordrecht, p. 111
Fischer D. A., Marcy G. W., 1992, ApJ, 396, 178
Foreman-Mackey D., 2016, J. Open Source Softw., 1, 24
Foreman-Mackey D., Hogg D. W., Lang D., Goodman J., 2013, PASP, 125, 306
Gaia Collaboration Brown A. G. A, Vallenari A., Prusti T., de Bruijne J. H. J., Babusiaux C., Bailer-Jones C. A. L., 2018, preprint (arXiv:1804.09365)
Gaia Collaboration et al., 2016, A&A, 595, A2
Gillen E., Hillenbrand L. A., David T. J., Aigrain S., Rebull L., Stauffer J., Cody A. M., Queloz D., 2017, ApJ, 849, 11
Gillon M. et al., 2012, A&A, 542, A4
Gillon M. et al., 2013, A&A, 552, A82
Gray D. F., 1989, PASP, 101, 832
Günther M. N., Queloz D., Demory B.-O., Bouchy F., 2017a, MNRAS, 465, 3379
Günther M. N. et al., 2017b, MNRAS, 472, 295

Hartman J. D., Bakos G. Á., Torres G., 2011, Eur. Phys. J. Web Conf, 11, 02002
Henden A., Munari U., 2014, Contrib. Astron. Obs. Skalnate Pleso, 43, 518
Hunter J. D., 2007, Comput. Sci. Eng., 9, 90
Husser T.-O., Wende-von Berg S., Dreizler S., Homeier D., Reiners A., Barman T., Hauschildt P. H., 2013, A&A, 553, A6
Irwin J. M. et al., 2011, ApJ, 742, 123
Jones E. et al., 2001, SciPy: Open Source Scientific tools for Python. Available at: http://www.scipy.org/ (online 2018 March 09)
Kovács G., Zucker S., Mazeh T., 2002, A&A, 391, 369
Latham D. W. et al., 2009, ApJ, 704, 1107
Mandel K., Agol E., 2002, ApJ, 580, L171
Mayor M. et al., 2003, The Messenger, 114, 20
McCauliff S. D. et al., 2015, ApJ, 806, 6
McCormac J., Pollacco D., Skillen I., Faedi F., Todd I., Watson C. A., 2013, PASP, 125, 548
McKinney W., 2010, in van der Walt S., Millman J., eds, Proceedings of the 9th Python in Science Conference, SciPy, Austin, p. 51
Milne E. A., 1926, MNRAS, 87, 43
Morton T. D., 2012, ApJ, 761, 6
Pecaut M. J., Mamajek E. E., 2013, ApJS, 208, 9
Popper D. M., Etzel P. B., 1981, AJ, 86, 102
Queloz D. et al., 2001, A&A, 379, 279
Raghavan D. et al., 2010, ApJ, 190, 1
Ricker G. R. et al., 2014, Proc. SPIE, 9143, 914320
Rossum G., 1995, Technical Report, Python Reference Manual, Amsterdam, The Netherlands
Santerne A. et al., 2015, MNRAS, 451, 2337
Santos N. C. et al., 2002, A&A, 392, 215
Schwarz R., Funk B., Zechner R., Bazsó Á., 2016, MNRAS, 460, 3598
Sekiguchi M., Fukugita M., 2000, AJ, 120, 1072
Skrutskie M. F. et al., 2006, AJ, 131, 1163
Sousa S. G. et al., 2008, A&A, 487, 373
Southworth J., Maxted P. F. L., Smalley B., 2004a, MNRAS, 351, 1277
Southworth J., Zucker S., Maxted P. F. L., Smalley B., 2004b, MNRAS, 355, 986
Stetson P. B., 1987, PASP, 99, 191
STScI Development Team 2013, Astrophysics Source Code Library, record ascl:1303.023
Tamuz O., Mazeh T., Zucker S., 2005, MNRAS, 356, 1466
Tokovinin A., Kiyaeva O., 2016, MNRAS, 456, 2070
Toner C. G., Gray D. F., 1988, ApJ, 334, 1008
Torres G., Andersen J., Giménez A., 2010a, A&AR, 18, 67
Torres G. et al., 2010b, ApJ, 727, 24
Torres G. et al., 2015, ApJ, 800, 99
van der Walt S., Colbert S. C., Varoquaux G., 2011, Comput. Sci. Eng., 13, 22
Ward-Duong K. et al., 2015, MNRAS, 449, 2618
Wheatley P. J. et al., 2018, MNRAS, 475, 4476
Wright E. L. et al., 2010, AJ, 140, 1868
Zacharias N., Finch C., Frouard J., 2017, AJ, 153, 166
Armstrong D. J. et al., 2018, MNRAS, sty1313

SUPPORTING INFORMATION

Supplementary data are available at *MNRAS* online.

NGTS photometry and centroid data for NGTS-3 (example in Table 2).
SPECULOOS photometry for NGTS-3 (example of Callisto *r*'-band photometry in Table 3).
HARPS RVs for NGTS-3 as retrieved by the standard data reduction software (HARPS DRS 3.5; example in Table 4).
HARPS RVs for NGTS-3 as retrieved by the BLENDFITTER software.
Animated version of Figure 5.
Please note: Oxford University Press is not responsible for the content or functionality of any supporting materials supplied by the authors. Any queries (other than missing material) should be directed to the corresponding author for the article.

[1]*Astrophysics Group, Cavendish Laboratory, J.J. Thomson Avenue, Cambridge CB3 0HE, UK*
[2]*Observatoire de Genève, Université de Genève, 51 Ch. des Maillettes, 1290 Sauverny, Switzerland*
[3]*Department of Physics, University of Warwick, Gibbet Hill Road, Coventry CV4 7AL, UK*
[4]*Centre for Exoplanets and Habitability, University of Warwick, Gibbet Hill Road, Coventry CV4 7AL, UK*
[5]*Astrophysics Group, Lennard-Jones Laboratories, Keele University, Staffordshire ST5 5BG, UK*
[6]*Space and Astronomy Department, Faculty of Science, King Abdulaziz University, 21589 Jeddah, Saudi Arabia*
[7]*King Abdullah Centre for Crescent Observations and Astronomy, Makkah Clock, Mecca 24231, Saudi Arabia*
[8]*Space sciences, Technologies and Astrophysics Research (STAR) Institute, Université de Liège, Allée du 6 Août 17, Bat. B5C, 4000 Liège, Belgium*
[9]*Department of Physics and Astronomy, Leicester Institute of Space and Earth Observation, University of Leicester, LE1 7RH, UK*
[10]*Institute of Planetary Research, German Aerospace Center, Rutherfordstrasse 2, D-12489 Berlin, Germany*
[11]*Center for Astronomy and Astrophysics, TU Berlin, Hardenbergstr. 36, D-10623 Berlin, Germany*
[12]*Astrophysics Research Centre, School of Mathematics and Physics, Queen's University Belfast, BT7 1NN Belfast, UK*
[13]*Departamento de Astronomía, Universidad de Chile, Casilla 36-D, Santiago, Chile*
[14]*Centro de Astrofísica y Tecnologías Afines (CATA), Casilla 36-D, Santiago, Chile*
[15]*Instituto de Astronomía, Angamos 0610, D-1272709, Antofagasta, Chile*
[16]*Institute of Geological Sciences, FU Berlin, Malteserstr. 74-100, D-12249 Berlin, Germany*

This paper has been typeset from a TEX/LATEX file prepared by the author.